Available online at www.sciencedirect.com

ScienceDirect

Underground Space 27 (2026) 236–258

www.keaipublishing.com/undsp

Research Paper

Comparative study on dynamic response and probabilistic seismic fragility of underground caverns under near-fault and far-field mainshock–aftershock sequences

Pengfei Chen [a,b], Quan Jiang [a,*], Yong Xia [c], Zhijun Liu [d], Long Li [a]

[a] *State Key Laboratory of Geomechanics and Geotechnical Engineering Safety, Institute of Rock and Soil Mechanics, Chinese Academy of Sciences, Wuhan 430071, China*
[b] *University of Chinese Academy of Sciences, Beijing 100049, China*
[c] *Chengdu Engineering Corporation Limited, Power China, Chengdu 610072, China*
[d] *College of Civil Engineering and Mechanics, Lanzhou University, Lanzhou 730000, China*

Received 3 September 2025; received in revised form 9 November 2025; accepted 17 November 2025
Available online 23 January 2026

Abstract

Actual seismic events typically exhibit mainshock–aftershock sequence characteristics, and source characteristics have a significant impact on cavern response. Currently, the influence of near-fault mainshock–aftershock sequences (NFMA) and far-field mainshock–aftershock sequences (FFMA) on underground caverns is generally ignored. This study aims to establish a framework for evaluating the dynamic response characteristics and seismic fragility of large-scale underground caverns under NFMA/FFMA. The response laws of residual displacement and rock fracture degree of cavern under NFMA/FFMA are comparatively studied, and the failure probability of different damage states is quantified by the fragility function. The results show that the surrounding rock of underground caverns exhibits significant cumulative damage effects and non-uniform failure characteristics under mainshock–aftershock sequences. Aftershock fragility is strongly related to the mainshock-damaged state for underground caverns. The collapse probability of underground caverns after 0.9*g* aftershocks in NFMA increased from 0.76% in slight damage to 21.12% in moderate damage and 53.51% in severe damage. This study can provide a probabilistic basis for seismic design, aftershock risk warning, and post-earthquake emergency assessment in underground engineering.

Keywords: Near-fault ground motion; Far-field ground motion; Mainshock–aftershock sequence; Rock fracture degree; Cumulative damage; Fragility analysis

1 Introduction

With the deepening development and utilization of underground space, the scale and complexity of large-scale underground cavern group have significantly increased, such as hydraulic underground powerhouses (Jiang et al., 2021), transportation tunnels (Xue et al., 2021), energy storage facilities (Liu et al., 2023), and mining roadway (Liu et al., 2025; Ma et al., 2025). Traditional theories suggest that underground caverns possess favorable seismic resilience. However, damage cases, such as the Daikai subway station (An et al., 1997), Du-Wen tunnel (Wang et al., 2009), Bolu double-hole tunnel (Jaramillo, 2017), Daliang tunnel (Chen et al., 2023), and the Yingliangbao (YLB) hydropower station (Chen et al., 2024), demonstrate that underground caverns can suffer damage under seismic loading, particularly in near-fault regions (Shen et al., 2014). Furthermore, actual seismic events predominantly occur as mainshock–aftershock

---

[*] Corresponding author.
E-mail address: qjiang@whrsm.ac.cn (Q. Jiang).

Peer review under the responsibility of Tongji University

https://doi.org/10.1016/j.undsp.2025.11.002
2467-9674/

sequences, where aftershocks can deliver a “secondary impact” to mainshock-damaged structures, potentially leading to cumulative damage. Such sequential ground motion poses a more severe challenge to cavern safety. Therefore, from the perspective of engineering lifecycle safety, quantitatively assessing cumulative damage evolution and fragility probabilities under mainshock–aftershock sequences, particularly near-fault/far-field scenarios, is crucial for optimizing seismic design and guiding post-earthquake emergency recovery.

The laws of cumulative damage and probabilistic seismic fragility are crucial for performance-based seismic design of infrastructure. Currently, scholars have conducted extensive and in-depth research on the seismic performance of ground structures under the mainshock–aftershock sequence, covering a wide range of aspects such as the cumulative damage mechanism (Zhang et al., 2019), the degradation of mechanical parameters induced by cyclic loads (Nouri et al., 2023), as well as the damping of dampers (Soureshjani & Lavassani, 2023; Rayegani et al., 2024) and structural fragility analysis (Bigdeli et al., 2025). In contrast, research on the dynamic response of large underground caverns under sequential earthquakes, particularly near-fault mainshock–aftershock sequences (NFMA), remains notably underdeveloped. Some scholars have realized the harmfulness of near-fault ground motion to underground caverns and have conducted relevant research (Chen et al., 2025; Xu et al., 2025). Shimizu et al. (2007) statistically analyzed numerous seismic damage cases of mountain tunnels in Japan, finding that tunnels within 10 km of the epicenter for magnitude 7 earthquakes or within 30 km for magnitude 8 earthquakes were more prone to severe damage. Qiu et al. (2019) analyzed the seismic response of large underground caverns under near-fault pulse ground motions, revealing that the long-period velocity pulses and high-frequency components of near-fault earthquakes caused more severe damage to underground structures. Sun et al. (2020) comparatively studied the nonlinear dynamic response of an arch tunnel under single mainshock excitation and mainshock–aftershock sequence excitation, and found that the mainshock–aftershock sequence would cause severe cumulative damage to the tunnel. Simultaneously, in terms of seismic performance assessment frameworks, fragility analysis under the performance-based earthquake engineering (PBEE) framework has been widely applied to various underground structures. Cui et al. (2023) established an automated assessment framework for seismic risks in subway stations by integrating Monte Carlo simulation and ontology theory, which comprehensively covers multiple indicators such as economic losses and casualties. Meng et al. (2024) proposed a rapid seismic resilience assessment framework for mountain tunnels considering topographic amplification effects and tunnel-soil dynamic interactions, and investigated the relationships among model geometric properties, material characteristics, and tunnel fragility. Xu et al. (2024) proposed a method for analyzing the seismic fragility of underground structures by integrating fuzzy random theory with the copula function, which can consider the fuzziness of multiple failure criteria and their correlations, revealing that the fuzziness of failure criteria has a significant impact on the vulnerability results. Huang et al. (2025) conducted a comparative study of fragility curves constructed from peak acceleration and tunnel drift under near-field non-pulse motion, near-field pulse motion, and far-field motion conditions for circular tunnels. The results show that circular tunnels are more likely to be destroyed under near-field pulse motion. The above studies expand the seismic stability analysis of underground caverns from the perspectives of dynamic response and fragility, revealing that seismic source characteristics and mainshock–aftershock sequences have significant effects on cavern stability. Despite these advancements, a critical scientific gap still exists: the current research mainly deals with source characteristics (near-fault/far-field) and sequence effects in isolation. The coupled effects of these two factors on the dynamic response mechanisms, cumulative damage evolution, and ultimate fragility of underground caverns are not yet systematically revealed or quantitatively compared.

Given the aforementioned research background and limitations, this study aims to systematically bridge the critical gap in understanding the coupled effects of seismic source characteristics (near-fault/far-field) and mainshock–aftershock sequences on underground caverns. To achieve this objective, a basic flow for evaluating the dynamic response characteristics and fragility of underground cavern group under NFMA/ far-field mainshock–aftershock sequences (FFMA) is established (Fig. 1). The specific research framework is as follows: First, representative near-fault and far-field seismic records are selected from the Pacific Earthquake Engineering Research Center (PEER) as ground motion inputs, and the ground motion is scaled according to incremental dynamic analysis (IDA) method to construct reasonable mainshock–aftershock sequences. Then, a three-dimensional numerical model is established based on the YLB underground cavern group, which experienced Luding M_S6.8 earthquake. The validity of the numerical model is verified by comparing the numerical simulation results with the field monitoring data. The residual displacement and rock fracture degree (RFD) of the caverns under two types of seismic sequences are comparatively analyzed to elucidate the cumulative damage effects. Subsequently, based on PBEE theory, fragility curves for NFMA and FFMA are developed and compared, quantifying the failure probability under different damage states and further investigating the impact of aftershocks on mainshock-damaged caverns. The results provide a deeper understanding of the seismic performance of underground caverns under different seismic scenarios and establish a more refined probability basis for performance-based seismic design.

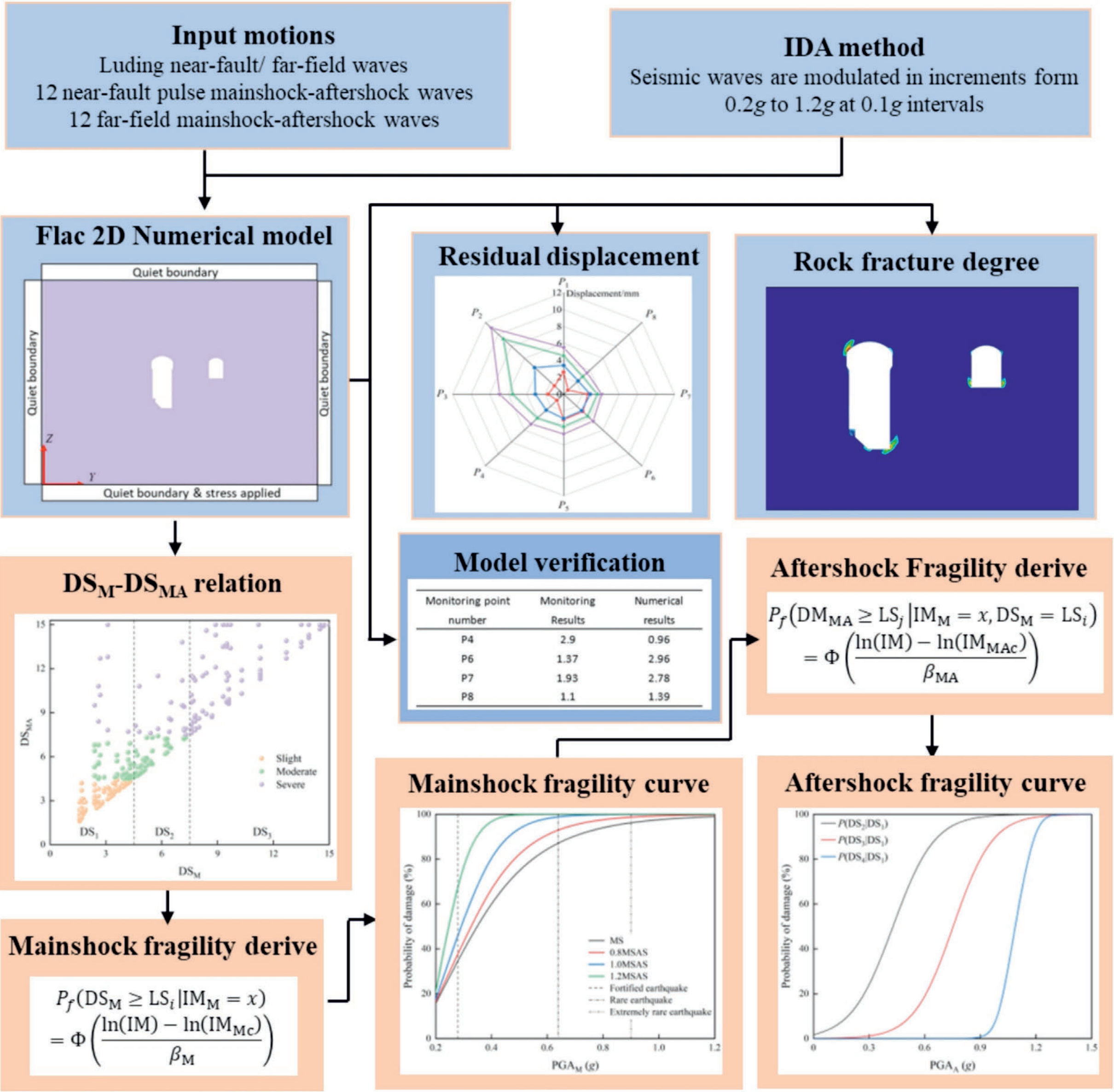

Monitoring point number	Monitoring Results	Numerical results
P4	2.9	0.96
P6	1.37	2.96
P7	1.93	2.78
P8	1.1	1.39

$$P_f(\mathrm{DM_{MA}} \geq \mathrm{LS}_j\,|\mathrm{IM_M} = x, \mathrm{DS_M} = \mathrm{LS}_i) = \Phi\left(\frac{\ln(\mathrm{IM}) - \ln(\mathrm{IM_{MAc}})}{\beta_{\mathrm{MA}}}\right)$$

$$P_f(\mathrm{DS_M} \geq \mathrm{LS}_i\,|\mathrm{IM_M} = x) = \Phi\left(\frac{\ln(\mathrm{IM}) - \ln(\mathrm{IM_{Mc}})}{\beta_{\mathrm{M}}}\right)$$

Fig. 1. Basic flow of dynamic response and fragility analysis of the underground cavern group under NFMA and FFMA.

2 Construction and input of mainshock–aftershock sequences

2.1 Ground motion selection

Earthquake ground motion characteristics significantly influence the dynamic response of underground caverns (Soureshjani & Massumi, 2019). Currently, there is no unified conclusion regarding the threshold for seismic source characteristics. Stewart et al. (2002) proposed that the threshold range of near-fault ground motion is less than 20–60 km, which has gained widespread acceptance. Sun et al. (2024) classified the earthquakes within the range of 20–60 km as near-field earthquakes when studying the tunnel earthquake damage. Zhu et al. (2025) also used this division concept when studying the residual displacement of a viscous system under near-fault ground motion. Based on this convention and considering data availability, this study defines near-fault mainshocks as those with epicentral distances <20 km and far-field ground motions as those with distances >60 km. To ensure sufficient record quantity, the distance threshold for near-fault aftershocks is relaxed to 35 km. Additionally, aftershocks do not need to have pulse characteristics. The ground motion selection adheres to the following principles:

1. The mainshock and its largest aftershock must originate from the same seismic event and station.
2. The mainshock magnitude $M_S > 6.5$ and the aftershock $M_S > 5.0$.
3. The fault distance of near-fault mainshocks must be ≤20 km, and that of aftershocks ≤35 km; far-field motions must have fault distances >60 km.
4. Near-fault mainshocks must exhibit pulse characteristics.

(5) Shear wave velocity $V_{30} > 250$ m/s.
(6) Mainshock peak ground acceleration ($\mathrm{PGA_M}$) $\geq 0.1g$.

Studies indicate that 10–20 ground motion records are sufficient to characterize uncertainties in incremental dynamic analysis. According to the above ground motion selection criteria, 12 near-fault pulse and 12 far-field non-pulse ground motion records are selected from the PEER strong motion database. Basic information is shown in Table 1.

2.2 Ground motion spectral analysis

To analyze the differences of seismic characteristics between NFMA and FFMA, the comparison curves of response spectra and mean spectra for NFMA/FFMA are plotted, as shown in Fig. 2. Figure 2(a) indicates that the near-fault mainshock response spectrum peaks at $T \approx 0.3$ s, while the aftershock response spectrum peaks at $T \approx 0.2$ s, with maximum spectral values of approximately $2.25g$ and $0.51g$, respectively. This demonstrates

Table 1
Basic information of selected ground motions.

Earthquake type	ID	Station name	Record sequence number	Magnitude M_W	Epicentral distance (km)	Duration (s)	Pulse period (s)
Near-fault	1	Bagnoli Irpinio	285	6.9	8.14	19.6	1.71
			296	6.2	17.79	21.8	–
	2	Newhall-Fire Station	1044	6.69	3.16	5.9	1.37
			1665	6.05	7.36	12.5	–
	3	Pacoima Kagel Canyon	1052	6.69	5.26	10.1	0.73
			1666	6.05	6.61	7.1	–
	4	CHY024	1193	7.62	9.62	27	6.65
			3264	6.3	29.49	14.2	–
	5	Sturno (STN)	292	6.9	6.78	15.2	3.27
			303	6.2	20.38	13.9	–
	6	TCU076	1511	7.62	2.74	29.5	4.73
			3472	6.3	23.84	17.6	–
	7	TCU082	1515	7.62	5.16	27	8.1
			3477	6.3	29.52	18.3	–
	8	CHY101	1244	7.62	9.94	30.4	5.34
			3317	6.3	34.55	22.3	–
	9	TCU049	1489	7.62	3.76	22.7	10.22
			3456	6.3	30.44	22.4	–
	10	TCU051	1491	7.62	7.64	28.9	10.38
			3458	6.3	32.36	20.3	–
	11	TCU053	1493	7.62	5.95	27.7	13.12
			3460	6.3	33.14	18.4	–
	12	TCU056	1496	7.62	10.48	31.8	8.94
			3461	6.3	34.7	19.8	–
Far-field	1	HWA045	1292	7.62	60.2	13.5	–
			3354	6.3	75.03	19.3	
	2	ILA024	1322	7.62	64.79	27.9	–
			3378	6.3	88.67	23.2	
	3	Anacapa Island	943	6.69	65.84	13.2	–
			1691	5.28	81.9	19.6	
	4	CHY022	1191	7.62	63.21	39.8	–
			3263	6.3	89.44	17.8	
	5	TTN004	1560	7.62	63.81	44.6	–
			3518	6.3	91.5	28.1	
	6	Rancho Cucamonga	1060	6.69	79.83	15.4	–
			1727	5.28	80.45	13.3	
	7	ILA010	1315	7.62	77.64	29.2	–
			3370	6.3	99.08	24.1	
	8	KAU012	1358	7.62	83.71	39.6	–
			3397	6.3	110.11	26.1	
	9	TCU092	1522	7.62	87.67	32	–
			3483	6.3	115.3	27.3	
	10	SMART1 C00	425	6.5	95.57	15.3	–
			570	7.3	56.01	24	
	11	SMART1 E01	426	6.5	93.17	11.6	–
			571	7.3	53.31	19.5	
	12	TAP028	1424	7.62	94.73	27.3	–
			3422	6.3	120.55	26.3	

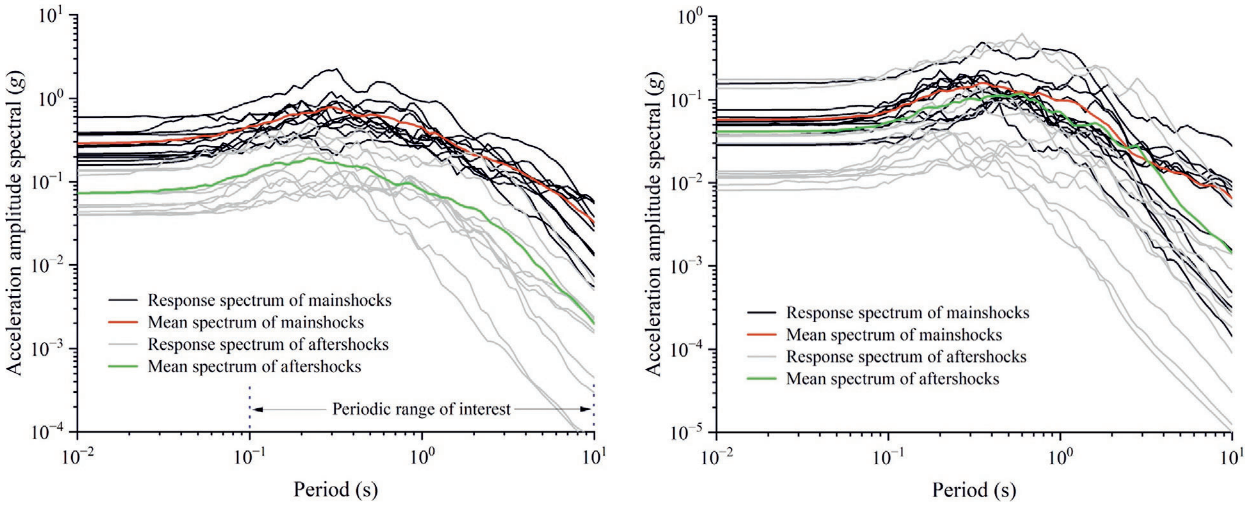

(a) (b)

Fig. 2. Acceleration response spectra of ground motions. (a) NFMA, and (b) FFMA.

that NFMA strongly excites short-period dynamic responses in caverns. Although the aftershock response spectrum is generally lower than the mainshock, certain period ranges exceed the mainshock spectrum, suggesting that aftershocks still pose potential threats to underground caverns in near-fault environments.

Compared to NFMA, FFMA attenuates faster with period and shows weaker amplification effects. Some aftershock response spectra in the far-field exceed the mainshock spectrum, primarily due to aftershocks of mainshock–aftershock sequence 10 and 11 having greater magnitudes than their corresponding mainshock. This phenomenon indicates that when aftershock magnitudes exceed the mainshock, even far-field conditions may trigger aftershock-dominated failures, so the uncertainty of the magnitude sequence should be considered in the design.

3 Numerical model

3.1 Engineering background

The underground cavern group of the YLB hydropower station is located within the left bank of the Dadu river in Luding county. The YLB engineering is located in the intersection of multiple faults and belongs to the seismic fortification zone of intensity VIII. In 2022, an $M_S6.8$ earthquake occurred in Luding, with the seismogenic fault identified as Moxi fault in the southeastern segment of the Xianshuihe fault. The YLB hydropower station is approximately 10 km straight-line distance from the epicenter and is located within the VIII intensity zone.

Seismic geological hazards in the YLB area exhibit distinct spatiotemporal characteristics. Major geological hazards occurred with the mainshock, with minor damage after aftershocks. South of Dewei town, seismic geological hazards were well developed and severely damaging; while north of Dewei town, both the development and damage degree of seismic geological hazards gradually decreased. Subsequently, multiple aftershocks above magnitude 4.0 occurred in Luding area. The Luding earthquake sequence represents a typical mainshock–aftershock sequence (Fig. 3).

3.2 Model construction

Given that the axial length of the underground caverns significantly exceeds their cross-sectional dimensions, a plane strain model is adopted in this study. The plane strain model has high computational efficiency and has been proved to be effective in simulating the dynamic response of the cavern section (Yu & Chen, 2021; Antoniou et al., 2023). Lv et al. (2009) demonstrated that the two-dimensional numerical model could effectively reflect the local surrounding rock dynamic behavior of the three-dimensional model. A typical unit #4 cross-section of the YLB underground caverns is selected to establish a plane strain model including both the main powerhouse and main transformer chamber. The model dimension is 348 m × 260 m × 2 m (length × height × width).

The main steps of this simulation are as follows: firstly, initial stress fields (σ_x, σ_y, σ_z, τ_{yz}) are applied based on measured in-situ stress data. Then the analysis of cavern excavation is carried out to obtain the stress state before the earthquake. Then, based on the excavation model, the adjusted stress time histories of the mainshock–aftershock sequences are vertically input from the bottom of the model. Quiet boundaries are applied to the top, bottom, and sides to suppress boundary reflection waves, as shown in Fig. 4(a).

According to the monitoring points arranged in the YLB underground cavern, displacement monitoring points

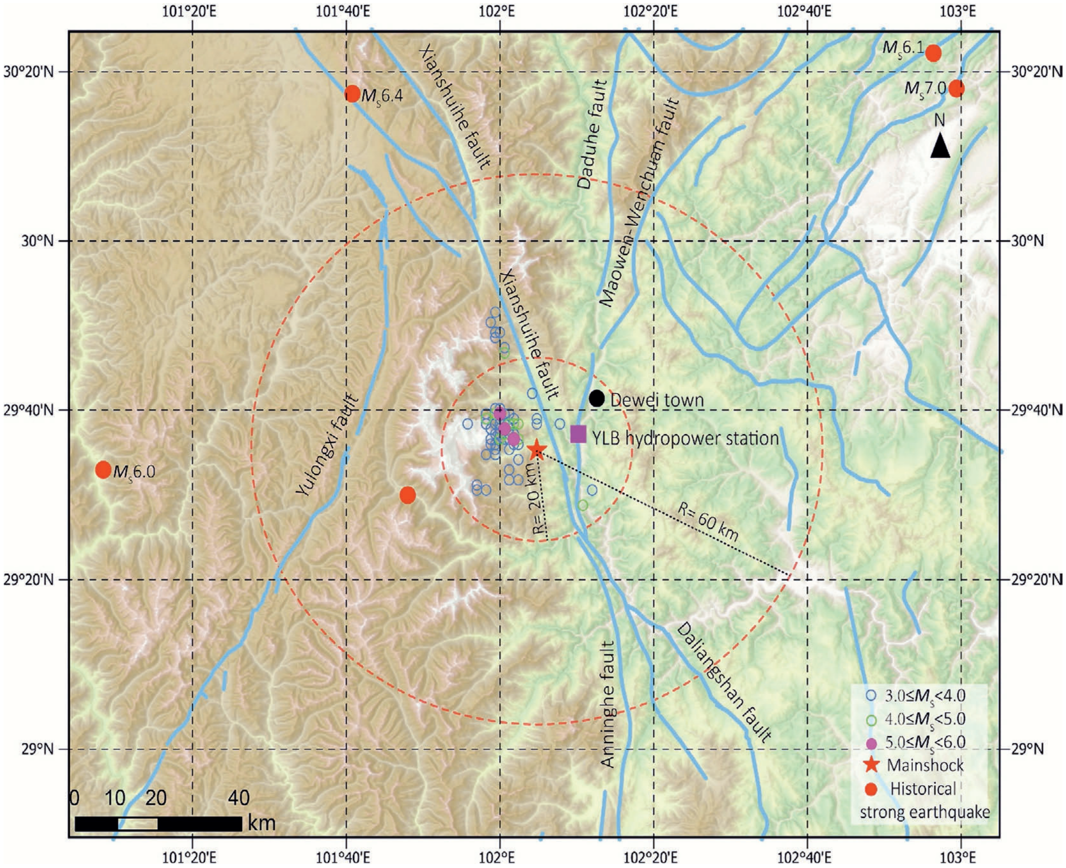

Fig. 3. Map of the distribution of the Luding earthquake and area tectonics.

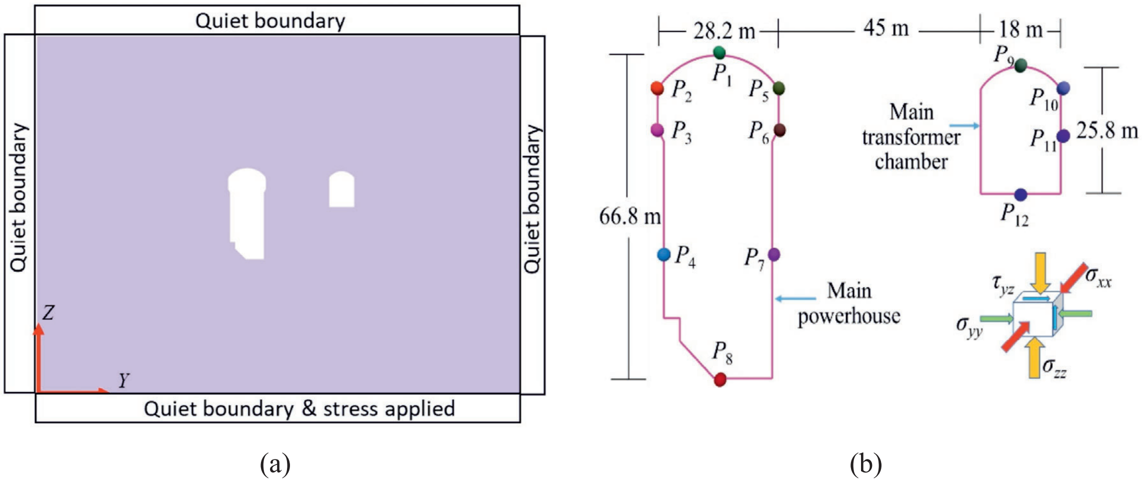

Fig. 4. YLB underground cavern model. (a) Dynamic boundary, and (b) location of monitoring points.

are set at the same position in the numerical model to monitor the displacement of the cavern group during the calculation process (Fig. 4(b)). Local damping is employed, and the value is 0.1256. The rock mass degradation mechanical model is adopted. Detailed mechanical parameters refer to the literature (Chen et al., 2024). The simulation assumes the most unfavorable scenario of full-face excavation without support.

3.3 Simulation scheme

Seismic sequence observations indicate that strong mainshocks are often followed by multiple aftershocks. Statistical studies show that most aftershocks have magnitudes lower than the mainshock, typically about 1.2 magnitude units lower (Bath, 1965). However, actual seismic sequence (e.g., the 2016 Kumamoto seismic sequence, 2018 Lombok seismic sequence, 2019 Ridgecrest seismic sequence, and 2023 Herat seismic sequence (Zhao & Liu, 2016; Lozos & Harris, 2020; Sasmi et al., 2023; Fu et al., 2025)) confirms that subsequent ground motion intensity may be equal to or even exceed the mainshock. Given that current technology cannot predict whether a secondary strong earthquake will occur after a strong earthquake, it is necessary to consider the amplification effects of subsequent ground motions in seismic analysis. Therefore, this study sets the upper limit of 1.2 times the $\mathrm{PGA_M}$ for aftershock peak ground acceleration ($\mathrm{PGA_A}$) to cover extreme scenarios, ensuring the comprehensiveness of cavern seismic evaluation.

Based on the IDA framework, 24 mainshock-aftershock sequences are constructed to evaluate the seismic performance of cavern group. The peak ground acceleration (PGA) is used as the scaling basis. The PGA of the ground motions is scaled in $0.1g$ increments from $0.2g$ to $1.2g$. The mainshock–aftershock intensity ratio parameter $\alpha = \mathrm{PGA_A} / \mathrm{PGA_M}$ is defined. For each mainshock intensity level, $\alpha = 0.8$, 1.0, and 1.2 are adopted to represent weakening, equal intensity, and amplification, respectively. Scaled mainshock and aftershock acceleration time histories are combined to form mainshock–aftershock sequences. For clarity, the seismic conditions are abbreviated as mainshock only (MS), mainshock–aftershock sequence with $\alpha = 0.8$ (0.8MSAS), and so forth. In order to keep the cavern in a balanced position before aftershock excitation, free ground motion with a certain time interval is often added between the mainshock and the aftershock. Research indicates that the time interval between mainshocks and aftershocks has minimal impact on cavern dynamic responses, and the time interval between earthquakes can be determined as needed (Pu & Li, 2023; Liu et al., 2024). Thus, a 5 s interval is applied between the mainshock and the aftershock. The mainshock–aftershock sequences are constructed in the form of mainshock +5 s interval + aftershock.

4 Nonlinear dynamic response of underground caverns

In this section, Luding earthquake data will be selected to construct two types of mainshock–aftershock sequence: NFMA and FFMA. The nonlinear dynamic behavior of underground caverns under NFMA and FFMA excitation will be introduced and discussed, and response parameters such as residual displacement and RFD will be studied.

4.1 Construction of Luding mainshock–aftershock sequences

On September 5, 2022, an $M_S6.8$ earthquake occurred in Luding county, followed by an $M_S5.6$ strong aftershock on January 26, 2023, which was the largest in terms of magnitude to date. Based on these events, representative NFMA and FFMA sequences are constructed using records from the China Earthquake Science Data Center. The near-fault records are selected from station 51LDJ, with an epicentral distance of 11.66 km and including pulse effects; the far-field records are taken from station 51HYW, with an epicentral distance of 90.51 km and a long duration. The sequence is constructed using the mainshock +5 s interval + aftershock combination mode. The corresponding acceleration time histories are shown in Fig. 5.

4.2 Model validation

To validate the effectiveness of the plane strain model and the reliability of numerical analysis, this study compares simulated residual displacements with field monitoring displacement of underground caverns after the $M_S6.8$ earthquake. The seismic record is input into the model for dynamic calculations. Then, the on-site monitoring

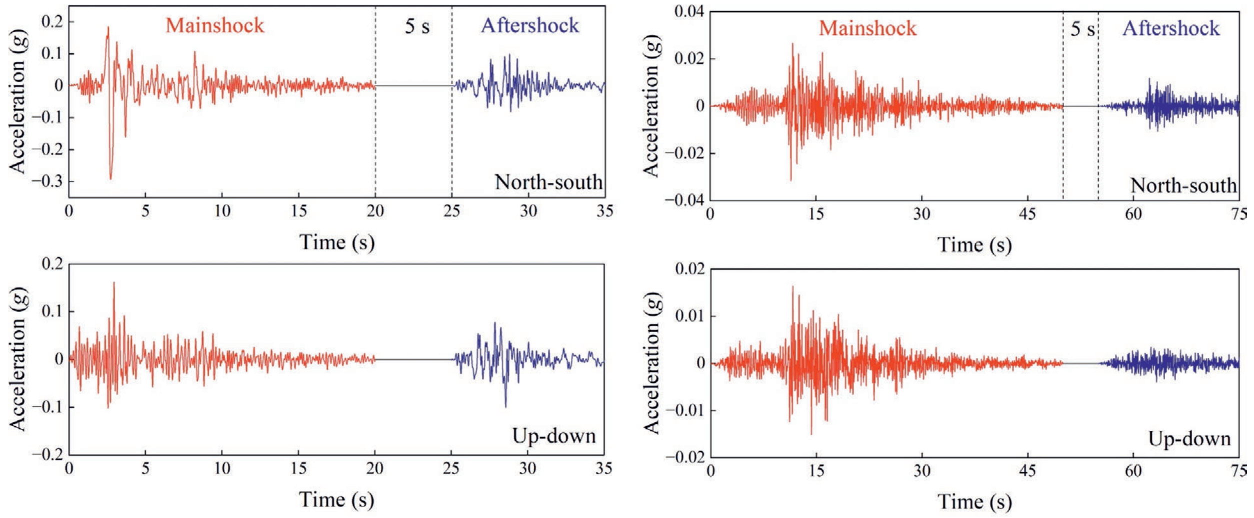

(a) (b)

Fig. 5. Acceleration time histories of Luding mainshock–aftershock sequences. (a) NFMA, and (b) FFMA.

data with the post-earthquake displacements from underground caverns greater than 1 mm are selected and compared with the residual displacements at the same locations in the model. The comparison results are shown in Table 2. It is critical to note that the values compared in Table 2 represent the incremental displacement induced purely by the seismic input, which starts from a post-excavation equilibrium state. The plane strain model results are in close agreement with field monitoring data, with the maximum error within 2 mm. Considering that the earthquake increment displacement is superimposed on the displacement caused by the larger excavation (about tens of millimeters), this error is acceptable on an engineering scale. Therefore, it can be concluded that the computational results of the plane strain model are valid.

4.3 RFD of surrounding rock

Accurate determination of the depth of the surrounding rock relaxation zone is of great significance for analyzing the stability of the surrounding rock in a large cavern. To align numerical simulation results with the depth of the surrounding rock relaxation zone observed in the field, Jiang et al. (2019) and Feng et al. (2022) proposed the index of RFD, which can not only directly characterize the fracture position and depth of the surrounding rock, but also quantitatively express the fracture degree of the surrounding rock. It is determined through true triaxial experiments that the surrounding rock enters a yield state when the RFD value exceeds 1. Through engineering examples and laboratory tests, the spatial distribution of RFD is consistent with the results of acoustic wave tests and borehole photography, which proves its effectiveness in extending from numerical results to engineering applications. RFD is defined as shown in Eq. (1).

$$\mathrm{RFD}=\begin{cases}\frac{q}{g(\theta_\sigma)\sqrt{Xp^2+Yp+Z}} & \text{(Pre-peak)}\\ 1+\varepsilon^{\mathrm{p}}_{\mathrm{s/t}}/\varepsilon^{\mathrm{p-lim}}_{\mathrm{s/t}} & \text{(Post-peak)}\end{cases}, \tag{1}$$

$$p=\frac{\sigma_1+\sigma_2+\sigma_3}{3}, \tag{2}$$

$$q=\sqrt{\frac{(\sigma_1-\sigma_2)^2+(\sigma_2-\sigma_3)^2+(\sigma_3-\sigma_1)^2}{2}}, \tag{3}$$

$$\mathrm{RFD}=\begin{cases}0.8-1 & \text{(Pre-peak fracture)}\\ 1-2 & \text{(Post-peak failure)}\\ 2 & \text{(Complete structural failure)}\end{cases}, \tag{4}$$

where σ_1, σ_2, and σ_3 are the maximum, medium, and minimum principal stresses respectively; X, Y, and Z are strength criterion coefficients; $g(\theta_\sigma)$ is the shape function on the deviatoric plane; $\varepsilon^{\mathrm{p}}_{\mathrm{s/t}}/\varepsilon^{\mathrm{p-lim}}_{\mathrm{s/t}}$ is the ratio of plastic strain to limit value. The range of RFD value is 0 to 2. If the value exceeds 2, set it to 2.

Table 2
Comparison of residual displacement from simulation and field monitoring (unit: mm).

Monitoring point number	Monitoring results	Numerical results
P_4	2.90	0.96
P_6	1.37	2.96
P_7	1.93	2.78
P_8	1.10	1.39

To better describe the distribution of RFD, this study focuses only on the yield zones of the surrounding rock where RFD exceeds 1. Tables 3 and 4, respectively, illustrate the characteristics of RFD distribution under NFMA and FFMA with $\mathrm{PGA_M}$ and $\mathrm{PGA_A}$ amplitude variations. It is worth noting that the color of RFD in Tables 3 and 4 represents the damage degree of the surrounding rock, and the redder the color of RFD, the greater the damage degree of the surrounding rock.

Overall, aftershocks exhibit a cumulative amplification and threshold effect on the RFD distribution for underground caverns. Under the same $\mathrm{PGA_M}$, comparing the four working conditions of MS ($\alpha = 0$), $\alpha = 0.8$, $\alpha = 1.0$, and $\alpha = 1.2$, it can be observed that under the re-excitation of low $\mathrm{PGA_A}$, the depth and range of RFD expansion of surrounding rock of cavern have increased to some extent, and with the increase of $\mathrm{PGA_A}$, the depth and area of RFD in cavern surrounding rock shows a significant upward trend. Specifically, when the $\mathrm{PGA_M}$ is between 0.2g and 0.4g, the RFD depth of the cavern surrounding rock is shallow and locally isolated. Even under the aftershock, the depth of RFD still changes little. When the $\mathrm{PGA_M}$ is between 0.6g and 0.8g, the RFD depth shows a certain degree of expansion. With the re-excitation of aftershocks, the RFD depth increases significantly, with cavern RFD still showing localized isolated distribution. When the $\mathrm{PGA_M} \geq 0.8g$, the RFD significantly expands, especially under $\alpha = 1.2$ conditions, where RFD tends to connect or has already connected to form bands. In some areas, the RFD depth approaches or even reaches the instability threshold, indicating that the surrounding rock of the cavern exhibits significant cumulative damage effects and potential local instability under the mainshock–aftershock sequence.

The comparison of results in Tables 3 and 4 indicates that the characteristics of seismic motion do not alter the locations of instability within the underground cavern. Regardless of whether subjected to NFMA or FFMA, the RFD distribution of the caverns is consistently concentrated at the left arch shoulder and right arch foot of the powerhouse, as well as the arch foot and sidewall of the main transformer chamber. However, it is evident that seismic motion characteristics significantly affect the extension depth of the RFD. Under MS ($\alpha = 0$) conditions, the differences in RFD distribution between NFMA and FFMA

Table 3
Evolution of RFD distribution under NFMA.

PGA_M	PGA_A			
	MS($\alpha = 0$)	$\alpha = 0.8$	$\alpha = 1.0$	$\alpha = 1.2$
0.2g	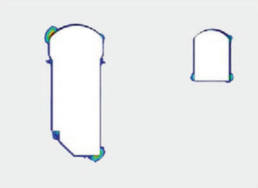	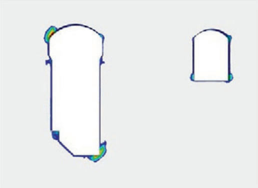	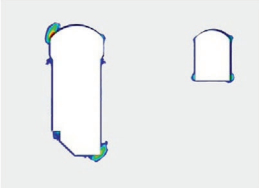	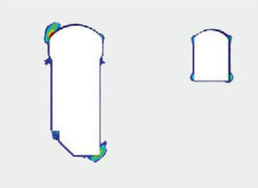
0.4g	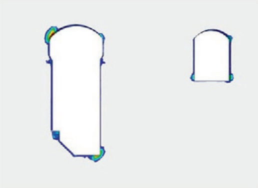	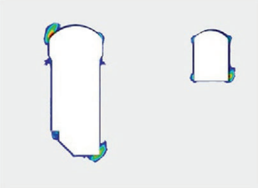	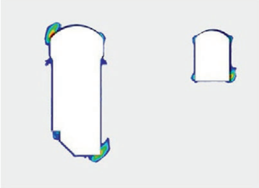	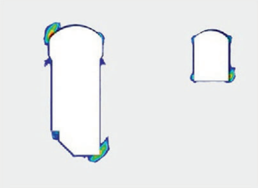
0.6g	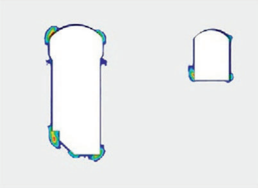	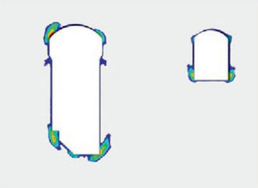	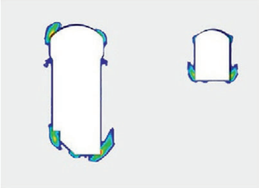	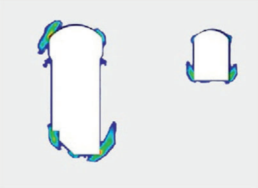
0.8g	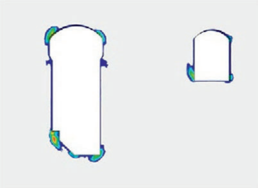	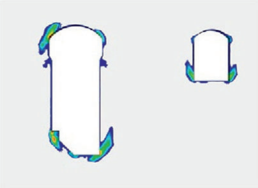	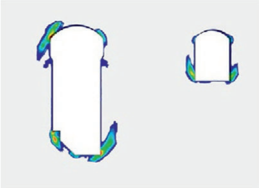	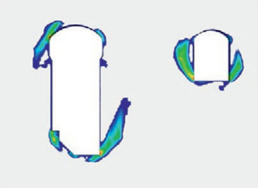
1.0g	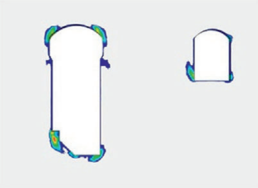	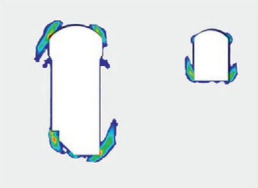	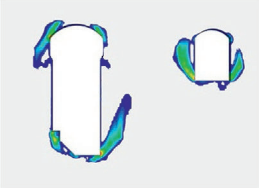	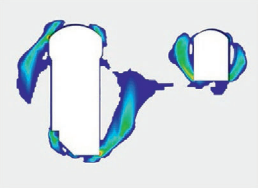
1.2g	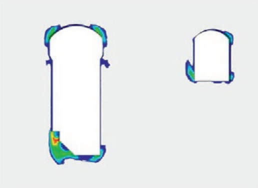	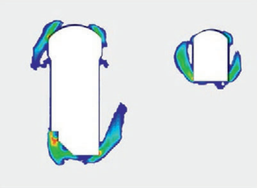	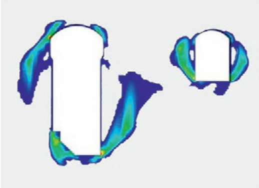	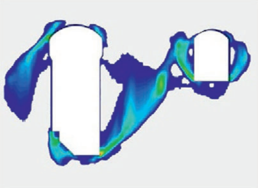

are relatively minor. With the excitation of aftershocks, NFMA exhibits more severe effects on the caverns. For instance, when the PGA_M of the NFMA is 1.2g, the RFD extension depths at the left arch foot of the main powerhouse reach 12.11 m and 27.69 m under $\alpha = 0.8$ and $\alpha = 1.0$, respectively. Particularly, under $\alpha = 1.2$, a continuous RFD band appears between caverns. In contrast, under FFMA with the PGA_M of 1.2g, the RFD extension depths at the left arch foot of the main powerhouse are 6.51, 6.53, and 15.91 m for $\alpha = 0.8$, $\alpha = 1.0$, and $\alpha = 1.2$, respectively.

4.4 Residual displacement of cavern surrounding rock

Figures 6 and 7, respectively, show the distribution curves of post-earthquake residual displacement of cavern surrounding rock varying with surrounding rock position under Luding NFMA and FFMA. As shown in the figures,

Table 4
Evolution of RFD distribution under FFMA.

PGA_M	PGA_A			
	MS($\alpha = 0$)	$\alpha = 0.8$	$\alpha = 1.0$	$\alpha = 1.2$
0.2*g*	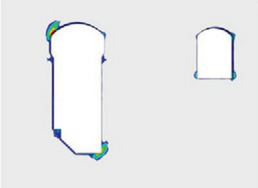	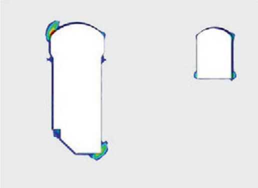	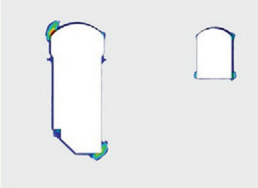	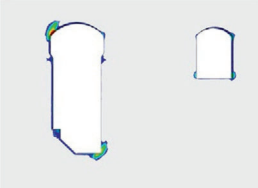
0.4*g*	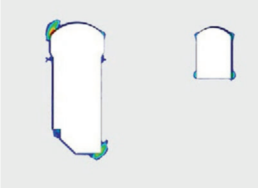	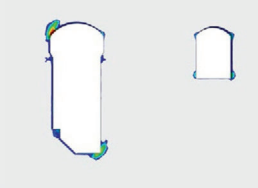	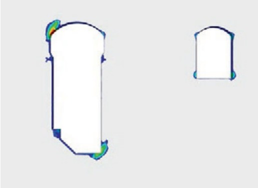	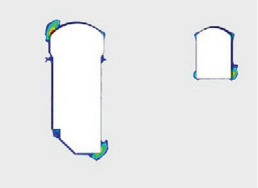
0.6*g*	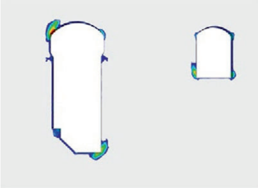	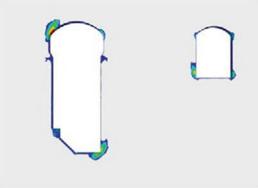	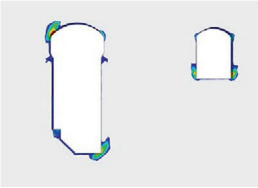	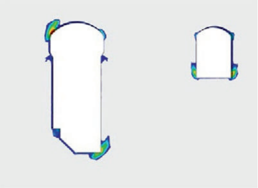
0.8*g*	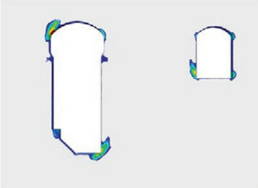	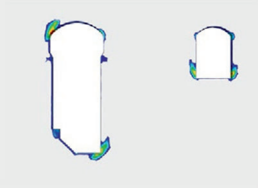	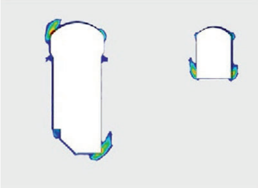	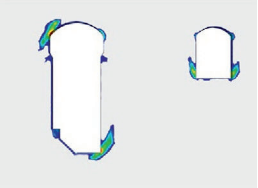
1.0*g*	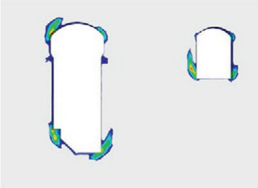	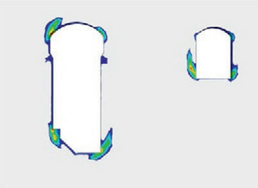	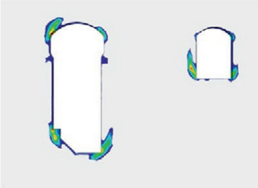	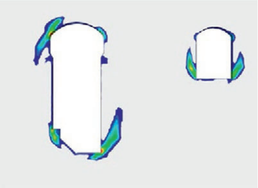
1.2*g*	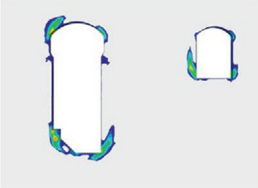	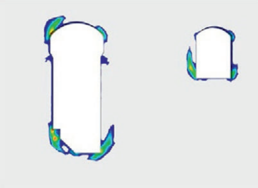	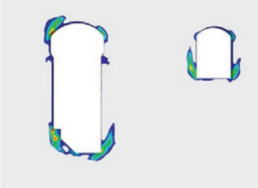	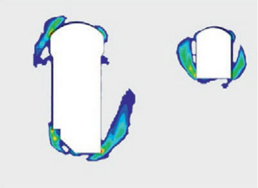

as PGA_M gradually increases from 0.2*g* to 1.2*g*, the residual displacement of cavern surrounding rock shows a clear increasing trend under both the NFMA and FFMA, indicating that mainshock intensity is an important factor controlling surrounding rock residual deformation. Under the same mainshock intensity, the superposition effect of aftershock sequences further amplifies the cumulative deformation of the surrounding rock. Taking monitoring point P_2 as an example, under NFMA, when PGA_M increases from 0.2*g* to 1.2*g*, residual displacement values increase from 1.39 mm to 19.99 mm. With aftershock excitation, residual displacements under the three conditions 0.8MSAS, 1.0MSAS, and 1.2MSAS at mainshock 1.2*g* reach 78.41, 123.34, and 151.29 mm, respectively. Under FFMA, when PGA_M increases from 0.2*g* to 1.2*g*, residual displacement values increase from 5.51 mm to 24.38 mm. With aftershock excitation, residual displacements under the three conditions 0.8MSAS, 1.0MSAS, and 1.2MSAS at mainshock 1.2g reach 39.84, 47.51, and 57.46 mm, respectively. It is noteworthy that residual displacement is not monotonically increasing; post-aftershock residual displacement may also be smaller than that of the mainshock. For example, when $\mathrm{PGA_M}$ under NFMA is 0.9g, the residual displacement at monitoring point P_5 after the mainshock is 15.31 mm, while the residual displacement under 0.8MSAS sequence is 7.22 mm. This may be due to the aftershock directionality being opposite to the mainshock, with aftershock excitation promoting surrounding rock movement in

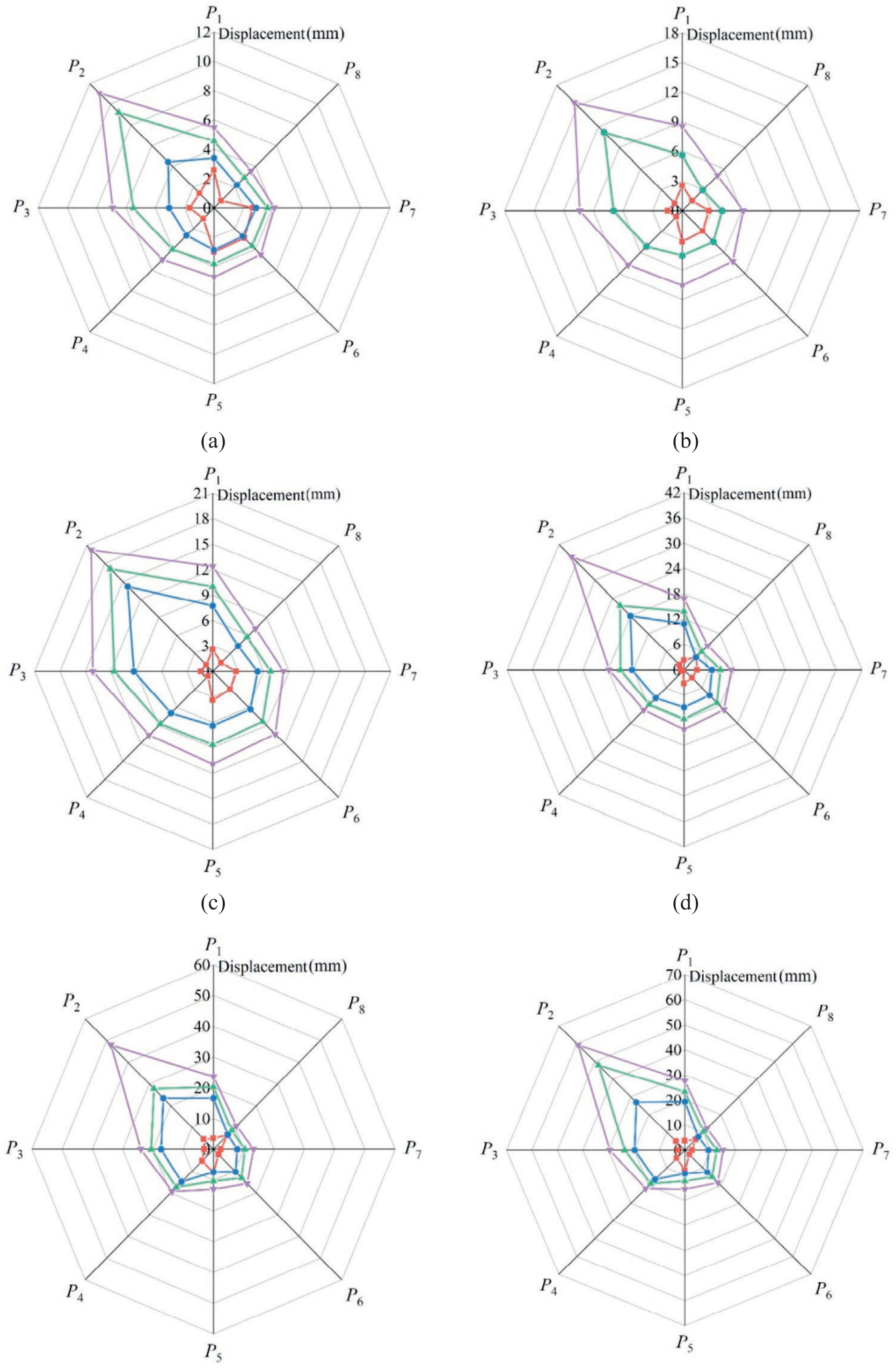

(a)

(b)

(c)

(d)

(e)

(f)

Fig. 6. Residual displacement after NFMA excitation. (a) $\mathrm{PGA_M} = 0.2g$, (b) $\mathrm{PGA_M} = 0.3g$, (c) $\mathrm{PGA_M} = 0.4g$, (d) $\mathrm{PGA_M} = 0.5g$, (e) $\mathrm{PGA_M} = 0.6g$, (f) $\mathrm{PGA_M} = 0.7g$, (g) $\mathrm{PGA_M} = 0.8g$, (h) $\mathrm{PGA_M} = 0.9g$, (i) $\mathrm{PGA_M} = 1.0g$, (j) $\mathrm{PGA_M} = 1.1g$, and (k) $\mathrm{PGA_M} = 1.2g$.

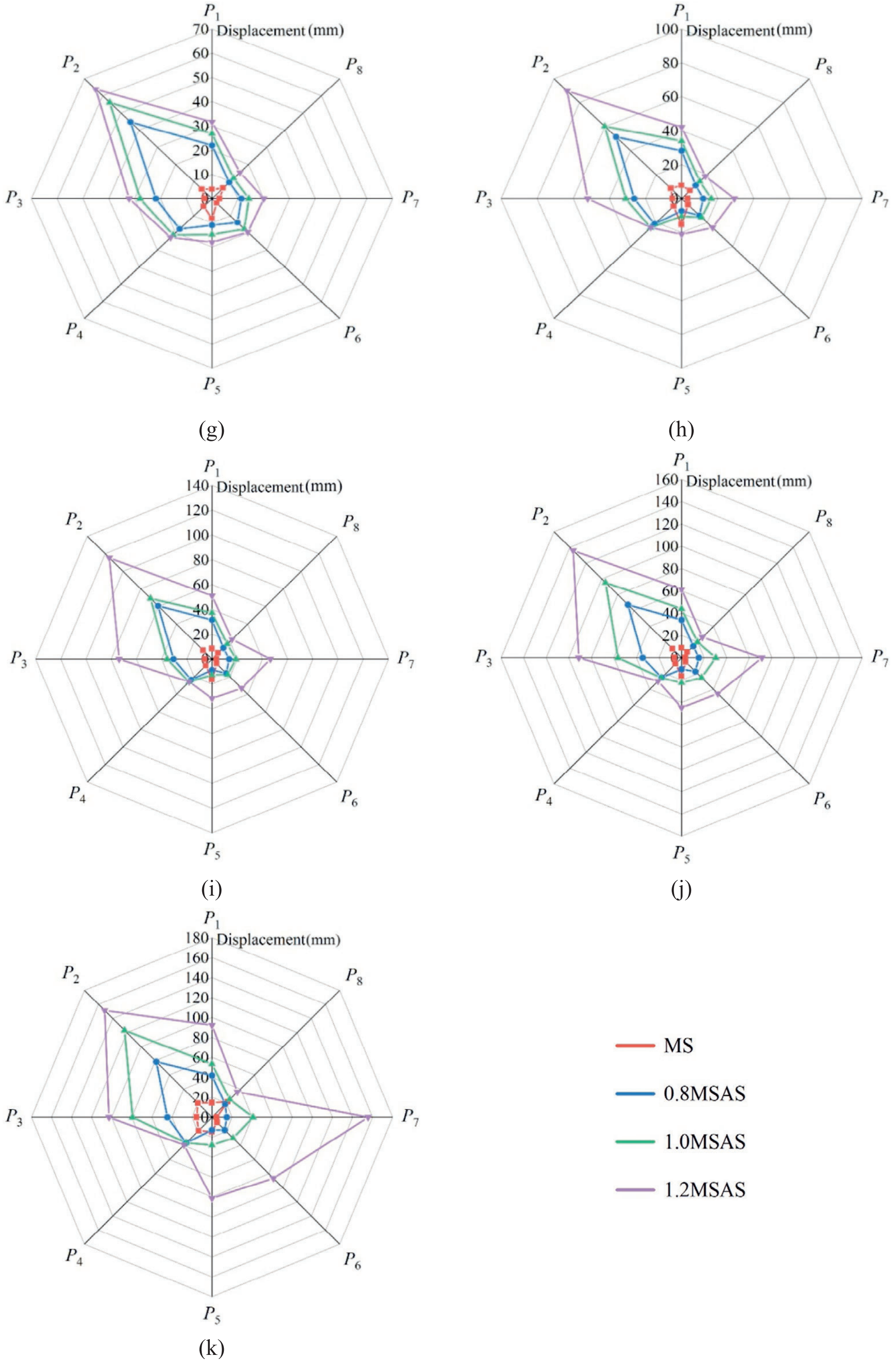

(g) (h) (i) (j) (k)

Fig 6. *(continued)*

the opposite direction, resulting in post-aftershock residual displacement being smaller than the mainshock.

5 Seismic fragility analysis of underground caverns

From the analysis in Section 4, it can be observed that different seismic sequences induce distinct nonlinear dynamic responses in underground caverns. Therefore, to reasonably assess the seismic performance of underground caverns, this section conducts a seismic fragility analysis from the perspective of failure probability based on extensive dynamic calculations. Furthermore, the influence of aftershocks on the fragility of mainshock-damaged caverns is quantified.

5.1 Mainshock–aftershock fragility analysis method

Seismic fragility is one of the core concepts in probabilistic seismic risk analysis, defined as the conditional probability that a cavern reaches or exceeds a specific limit state under given ground motion intensity. This function quantitatively describes how cavern damage evolves with increasing seismic intensity, providing a complete statistical characterization of the exceedance probabilities for all limit states, as indicated in Eq. (5).

$$P_{\mathrm{f}} = P[\mathrm{DS}_{\mathrm{M}} \geq \mathrm{LS}_i | \mathrm{IM}_{\mathrm{M}} = x], \tag{5}$$

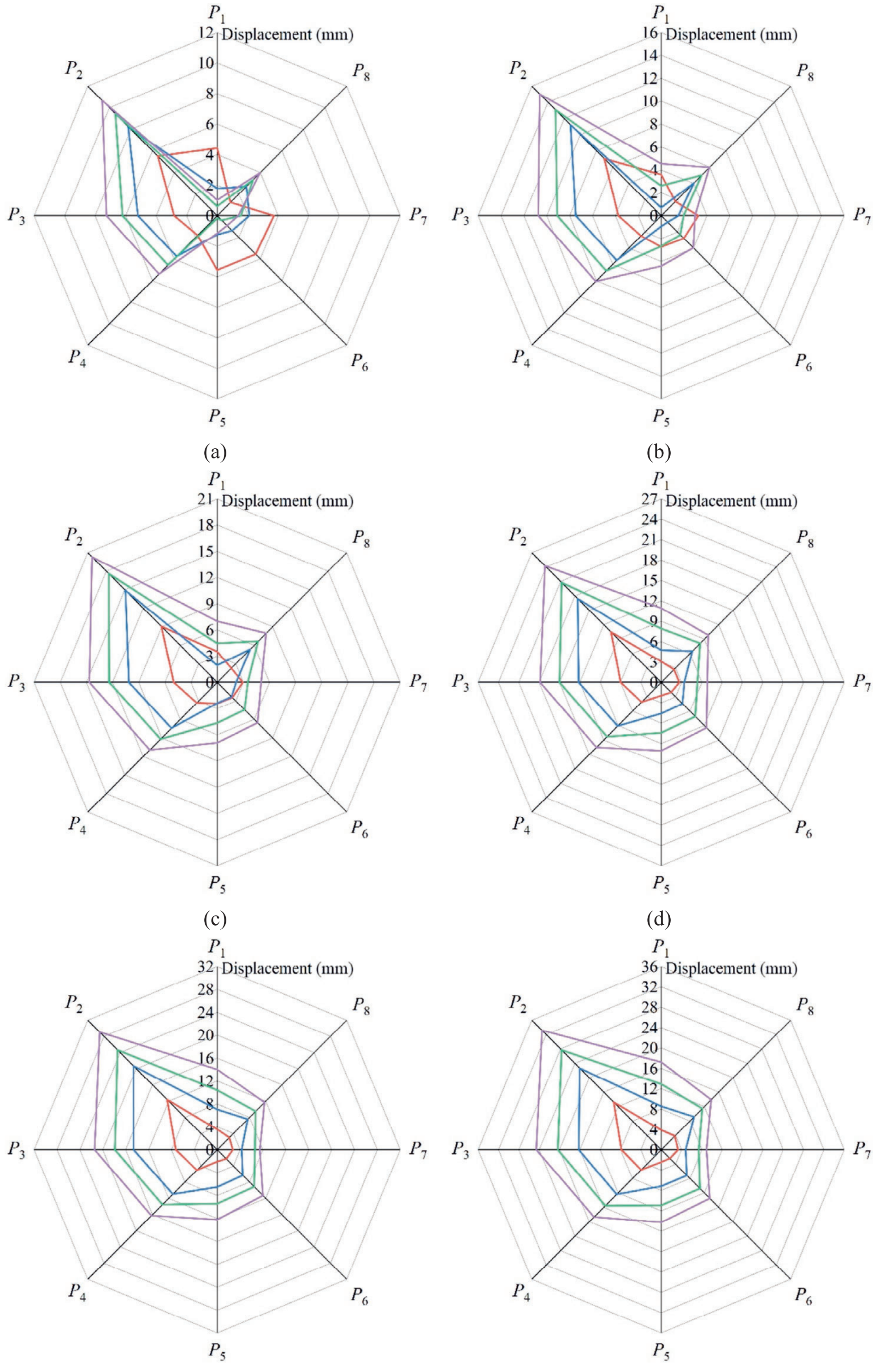

(a) (b)

(c) (d)

(e) (f)

Fig. 7. Residual displacement after FFMA excitation. (a) $\mathrm{PGA_M} = 0.2g$, (b) $\mathrm{PGA_M} = 0.3g$, (c) $\mathrm{PGA_M} = 0.4g$, (d) $\mathrm{PGA_M} = 0.5g$, (e) $\mathrm{PGA_M} = 0.6g$, (f) $\mathrm{PGA_M} = 0.7g$, (g) $\mathrm{PGA_M} = 0.8g$, (h) $\mathrm{PGA_M} = 0.9g$, (i) $\mathrm{PGA_M} = 1.0g$, (j) $\mathrm{PGA_M} = 1.1g$, and (k) $\mathrm{PGA_M} = 1.2g$.

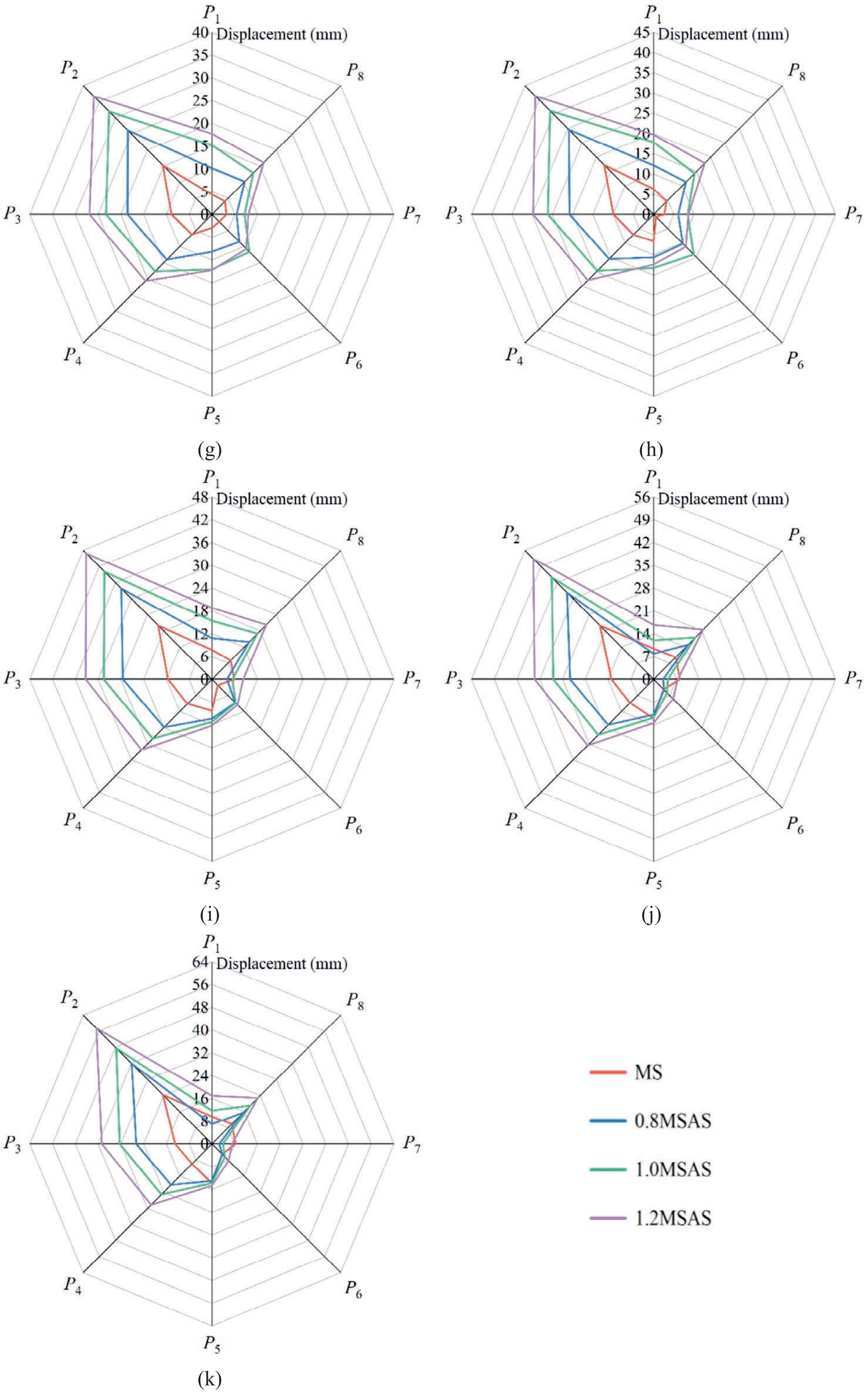

(g) (h)

(i) (j)

(k)

Fig 7. *(continued)*

where P_f is the fragility function; DS_M is the engineering demand measure under mainshock; LS_i is the ith performance level of the cavern; IM_M is the intensity measure of the mainshock; x is the intensity level of the ground motion.

Studies have shown that under given seismic intensity measure $IM_M = x$, the conditional probability that the engineering demand measure DS_M exceeds limit state LS_i typically follows a lognormal distribution. Therefore, the fragility function can be expressed as Eq. (6):

$$P_{\mathrm{f}}(\mathrm{DS}_{\mathrm{M}} \geq \mathrm{LS}_i | \mathrm{IM}_{\mathrm{M}} = x) = \Phi\left(\frac{\ln(\mathrm{IM}) - \ln(\mathrm{IM}_{\mathrm{MC}})}{\beta_{\mathrm{M}}}\right), \quad (6)$$

where Φ is the standard normal distribution function, $\mathrm{IM}_{\mathrm{MC}}$ is the critical intensity measure for the mainshock, and β_{M} is the logarithmic standard deviation of the mainshock fragility function.

Within the seismic fragility framework for underground caverns, the above seismic fragility function is termed the mainshock fragility function. Building upon this, the aftershock fragility function is developed by introducing post-mainshock damage state variables, as shown in Eq. (7). It quantifies the probability of a mainshock-damaged cavern transitioning to a more severe damage state under subsequent aftershock excitation.

$$P_{\mathrm{f}} = P\left[\mathrm{LS}_j | \mathrm{IM}_{\mathrm{MA}} = x, \mathrm{DS}_{\mathrm{M}} = \mathrm{LS}_i\right], \quad (7)$$

where LS_j is the jth performance level, generally $j \geq i$, indicating that aftershocks cause damage exceeding that of the mainshocks.

The relationship between the mainshock-aftershock sequence intensity measure $\mathrm{IM}_{\mathrm{MA}}$ and the cavern's mainshock-aftershock demand measure $\mathrm{DS}_{\mathrm{MA}}$ is shown in Eq. (8):

$$P_{\mathrm{f}}(\mathrm{DS}_{\mathrm{MA}} \geq \mathrm{LS}_j | \mathrm{IM}_{\mathrm{MA}} = x, \mathrm{DS}_{\mathrm{M}} = \mathrm{LS}_i) = \Phi\left(\frac{\ln(\mathrm{IM}) - \ln(\mathrm{IM}_{\mathrm{MAC}})}{\beta_{\mathrm{MA}}}\right), \quad (8)$$

where $\mathrm{IM}_{\mathrm{MAC}}$ is the critical intensity measure for aftershocks, and β_{MA} is the logarithmic standard deviation of the aftershock fragility function.

5.2 Classification of seismic performance levels

In seismic fragility analysis of underground engineering, a reasonable classification of damage states is crucial for establishing reliable fragility relationships. Considering the on-site support system for the surrounding rock of the YLB hydropower station underground cavern primarily employs anchor bolts with lengths of 6 and 9 m (as shown in Fig. 8), this study defines damage states based on RFD depth while incorporating anchor bolt characteristics to reflect the interaction between anchor bolts and the surrounding rock seismic response. Specifically, for the operational (OP) performance level, the depth of RFD should be less than the effective control range of 6 m anchor bolts. Considering the influence range is usually slightly smaller than the design length, the upper limit of OP state is set to 4.5 m. When the depth of RFD is between 4.5 m and the control capability of 9 m anchor bolts, anchor bolts partially fail but remain repairable, defined as the repairable (RP) state, with its upper threshold considering the reduction of the 9 m anchor bolt influence range, set at 7.5 m. When the depth of RFD exceeds 7.5 m, it shows that the support is completely ineffective, the cavern is in a life safety state (LS), and the depth of RFD above 7.5 m has obviously exceeded the bearing capacity of the anchor bolt. To define the limit state of potential life safety, the final threshold is set at 15 m, so as to represent the extreme situation that the cavern is close to collapse. The quantitative thresholds of each performance level under the condition of three-level fortification requirements are shown in Table 5.

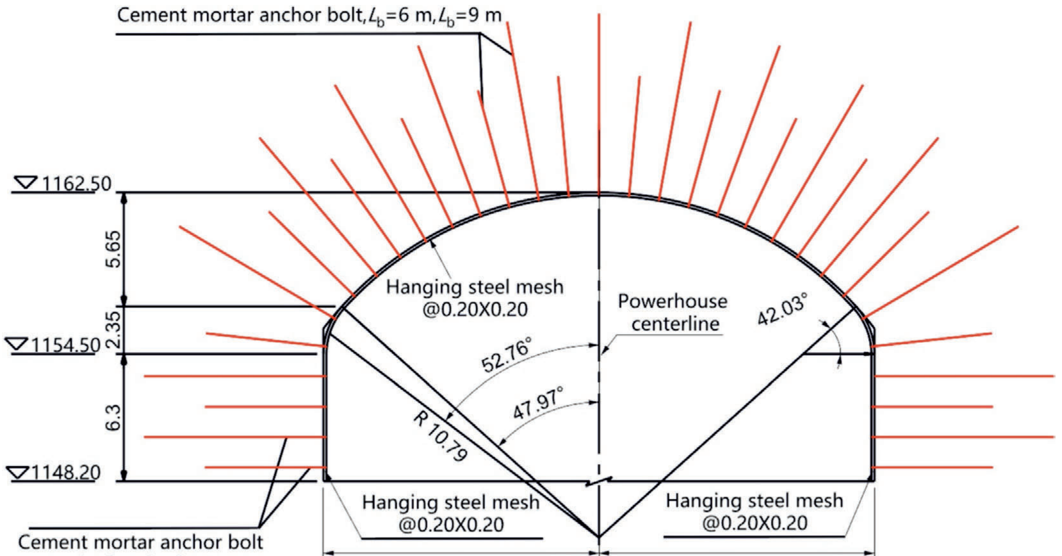

Fig. 8. Top anchor bolt support diagram of the YLB hydropower station main powerhouse. (Unit: m)

Table 5
Seismic performance levels of underground caverns based on RFD depth.

Design requirement	Performance level	Threshold L (m)
Level I	Operational	$L < 4.5$
Level II	Repairable	$4.5 \leq L < 7.5$
Level III	Life safety	$7.5 \leq L \leq 15$

Table 6
Seismic damage classification of underground caverns based on RFD depth.

Damage level	Threshold L (m)
Slight damage	$L < 4.5$
Moderate damage	$4.5 \leq L < 7.5$
Severe damage	$7.5 \leq L < 15$
Collapse	$L > 15$

Based on this classification, the seismic damage states of underground caverns are divided into four levels: slight damage, moderate damage, severe damage, and collapse, and the classification standard of seismic damage grade of cavern based on RFD is established. Specifically, when RFD < 4.5 m, the cavern is in a slight damage state; when 4.5 m ≤ RFD < 7.5 m, it is in a moderate damage state; when 7.5 m ≤ RFD < 15 m, it is in a severe damage state; when RFD ≥ 15 m, it is in a collapse state, as shown in Table 6.

5.3 Fragility analysis

PGA has become the principal strength parameter in most seismic design codes due to its advantages of strong correlation with dynamic response and easy extraction. In addition, PGA is often selected as the intensity measure in seismic fragility analysis (Guo et al., 2024; Cui et al.,

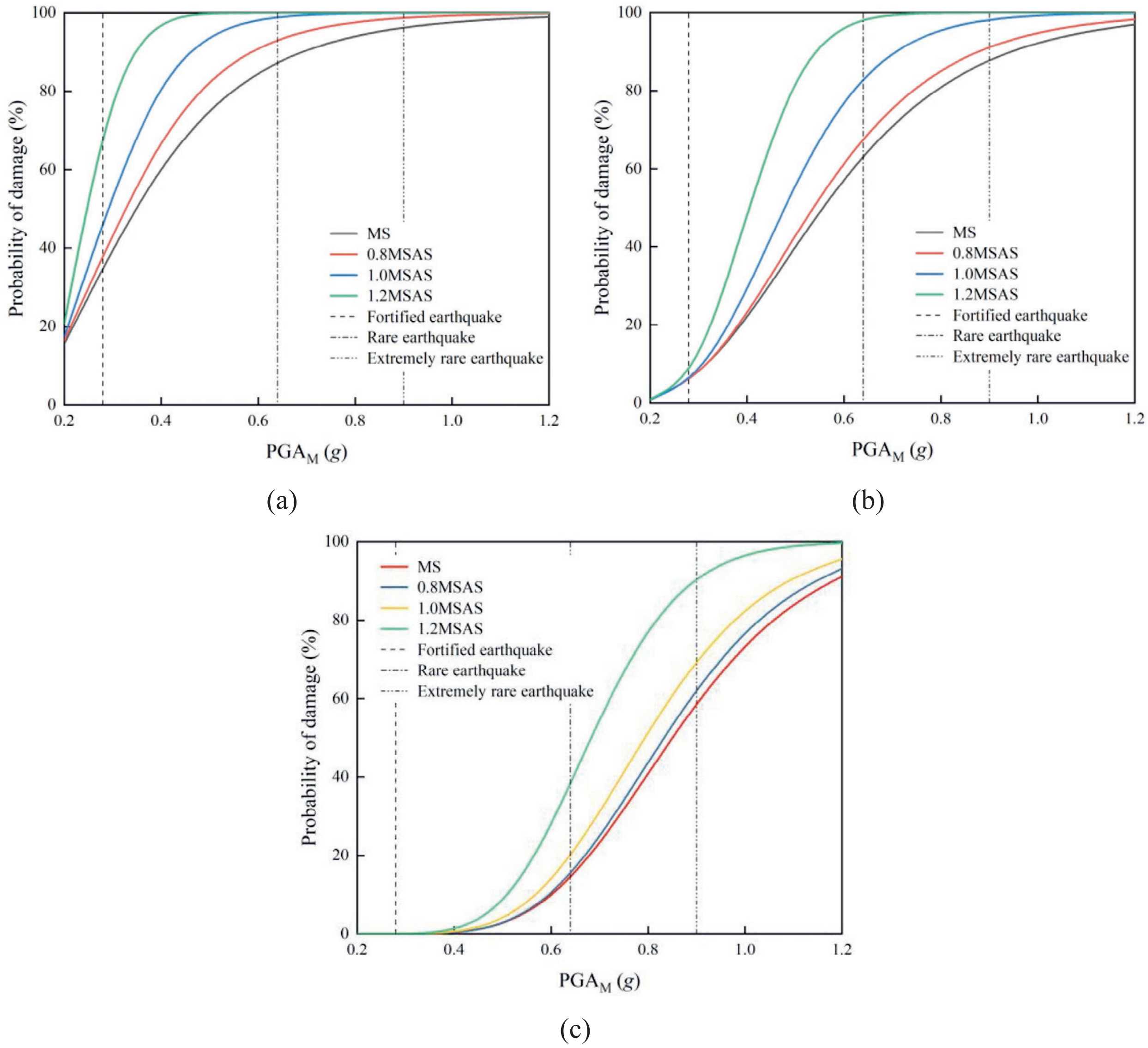

(a)

(b)

(c)

Fig. 9. Effect of varying aftershock intensities on failure probability under NFMA. (a) Operational, (b) repairable, and (c) life safety.

2025). Therefore, PGA is chosen as the intensity measure in this study. Based on Eq. (6), the probability that the near-fault and far-field ground motions of underground cavern reach three limit states under the action of the mainshock and mainshock–aftershock is calculated, and the seismic fragility curves for aftershocks of varying intensities are obtained (Figs. 9 and 10).

From the morphological characteristics of fragility curves, it can be observed that compared with the mainshock fragility curves, the mainshock–aftershock sequence curves shift leftward, and the magnitude of this shift increases with aftershock intensity. This phenomenon is evident across all three damage states, intuitively reflecting the cumulative effect of aftershocks on the damage probability of underground caverns. At the same PGA_M, the exceedance probability of fragility curves increases with increasing PGA_A.

For NFMA, each $0.1g$ increase in aftershock intensity results in an average exceedance probability increase of 54.74%, 46.55%, and 38.10% for the OP, RP, and LS states, respectively. For FFMA, the corresponding increases are 48.50%, 31.91%, and 17.37%. These results show that the influence of aftershocks on the fragility of underground caverns cannot be neglected, and only considering the mainshock in seismic assessment would obviously underestimate the cavern's dynamic response. It is particularly noteworthy that the damage probability of aftershocks to underground caverns is significantly different under different PGA and damage states of mainshock, which indicates that the damage probability of underground caverns under sequential ground motions is strongly dependent on the damage state of mainshock.

The exceedance probability of underground caverns under NFMA and FFMA is shown in Table 7. Under

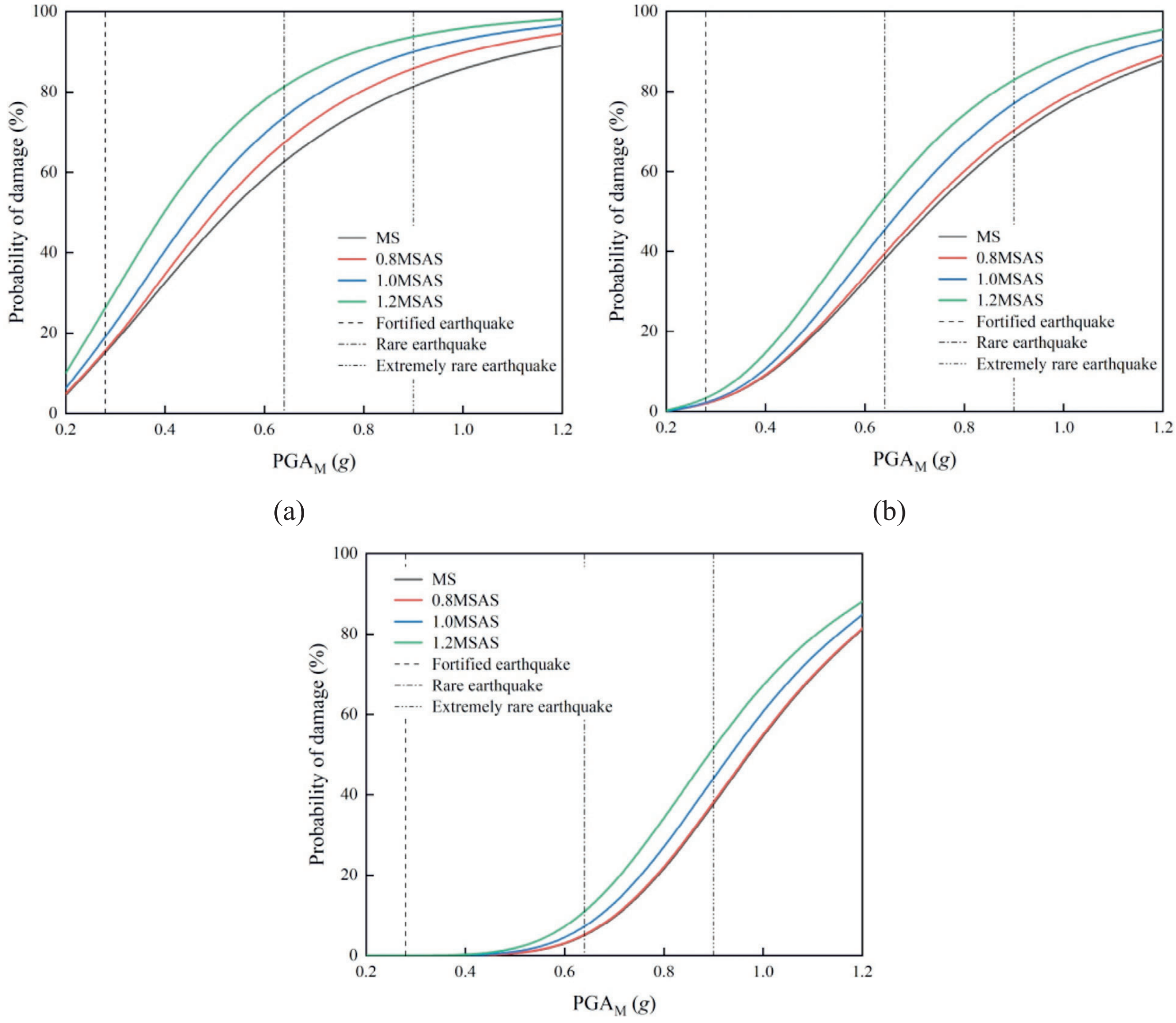

(a)

(b)

(c)

Fig. 10. Effect of varying aftershock intensities on failure probability under FFMA. (a) Operational, (b) repairable, and (c) life safety.

Table 7
Exceedance probability of underground caverns under different ground motion intensities under different ground motion.

Type	PGA_M (g)	Exceedance probability (%)											
		MS			0.8MSAS			1.0MSAS			1.2MSAS		
		OP	RP	LS	OP	RP	LS	OP	RP	LS	OP	RP	LS
Near-fault	0.2	15.56	0.67	0	16.41	0.79	0	17.27	0.88	0	20.81	0.93	0
	0.3	39.91	6.41	0	43.49	6.49	0	54.12	6.63	0	84.57	7.28	0
	0.4	61.08	21.46	0.16	68.21	22.40	0.16	83.32	28.20	0.25	98.98	48.76	0.44
	0.5	75.74	40.19	1.93	83.35	43.17	1.95	94.92	56.87	2.95	99.96	85.85	6.40
	0.6	85.05	57.72	8.77	91.50	62.06	9.27	98.55	78.40	12.75	100.00	97.60	26.65
	0.7	90.76	71.55	22.58	95.67	76.19	24.25	99.59	90.39	30.67	100.00	99.69	55.42
	0.8	94.24	81.43	40.87	97.78	85.62	43.81	99.88	96.02	51.73	100.00	99.97	78.65
	0.9	96.37	88.11	59.07	98.84	91.51	62.65	99.97	98.42	70.10	100.00	100.00	91.54
	1.0	97.68	92.46	73.93	99.39	95.05	77.35	99.99	99.38	83.15	100.00	100.00	97.09
	1.1	98.50	95.23	84.46	99.67	97.13	87.24	100.00	99.76	91.18	100.00	100.00	99.10
	1.2	99.02	96.99	91.21	99.82	98.34	93.20	100.00	99.91	95.63	100.00	100.00	99.74
Far-field	0.2	4.46	0.13	0	4.91	0.13	0	6.25	0.13	0	10.07	0.21	0
	0.3	17.68	1.97	0	17.99	1.97	0	22.01	2.16	0	30.34	3.39	0
	0.4	32.67	8.19	0.01	34.75	8.42	0.01	40.86	9.77	0.03	51.07	13.68	0.09
	0.5	46.90	19.11	0.27	50.56	19.81	0.30	57.47	23.24	0.55	67.25	29.90	1.20
	0.6	58.92	32.62	2.20	63.53	33.86	2.34	70.23	39.34	3.58	78.52	47.47	6.15
	0.7	68.50	46.32	8.55	73.46	47.97	8.89	79.41	54.73	12.06	85.99	62.88	17.43
	0.8	75.92	58.63	20.88	80.78	60.48	21.41	85.81	67.59	26.54	90.85	74.80	33.97
	0.9	81.59	68.85	37.54	86.09	70.72	38.12	90.20	77.45	44.21	93.98	83.34	51.95
	1.0	85.88	76.92	54.90	89.90	78.67	55.41	93.20	84.61	61.20	96.01	89.17	67.81
	1.1	89.13	83.09	69.91	92.64	84.63	70.28	95.26	89.63	74.97	97.32	93.03	79.85
	1.2	91.59	87.70	81.22	94.61	89.01	81.44	96.67	93.06	84.82	98.19	95.54	88.05
Difference in average exceedance probability		14.46			15.44			16.77			20.00		

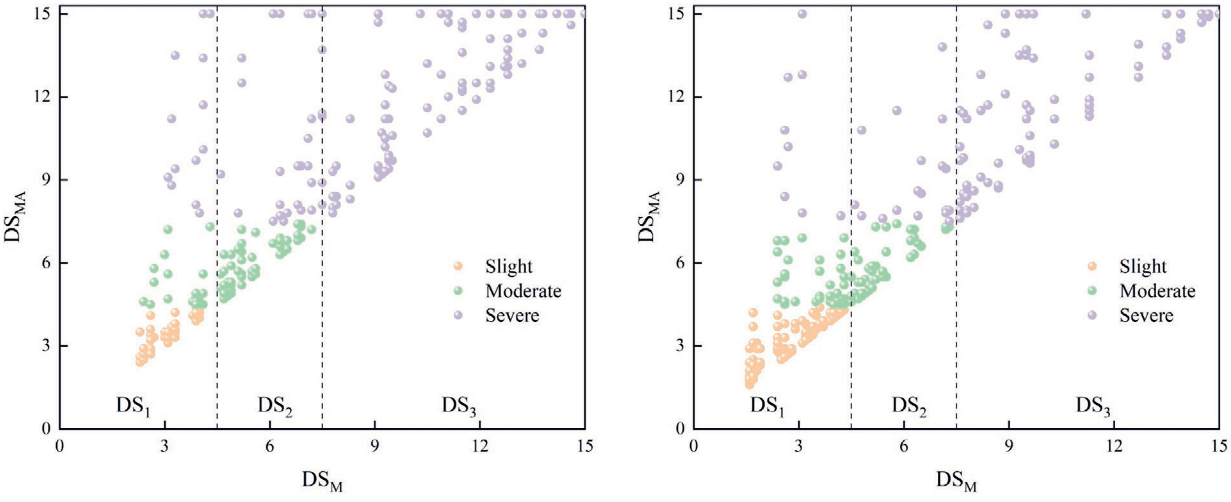

(a)

(b)

Fig. 11. Relationship between mainshock damage index DS_M and cumulative damage index DS_{MA} under sequence-type ground motion. (a) NFMA, and (b) FFMA.

the same PGA_M level, NFMA shows greater failure probability. For example, under NFMA, when the PGA_M is 0.4g in MS condition, the probabilities of exceeding the OP, RP, and LS levels are 61.08%, 21.46%, and 0.16%, respectively. Under FFMA at the same level, these probabilities are 32.67%, 8.19%, and only 0.01%, respectively. To more intuitively compare the differential effects of NFMA and FFMA on the probability of cavern failure, the probability difference between NFMA and FFMA is calculated for each condition at the same PGA_M. The arithmetic mean of this difference is computed over all analyzed PGA_M levels. Therefore, the average fragility probability under NFMA is found to be 14.46%, 15.44%, 16.77%, and 20.00% higher than that under FFMA for the four scenarios of $\alpha = 0$, $\alpha = 0.8$, $\alpha = 1.0$, and $\alpha = 1.2$, respectively. This indicates that the pulse characteristics and high-frequency components of NFMA induce more severe cumulative damage effects on underground caverns. These findings highlight the significant influence of ground motion characteristics on aftershock fragility assessment and provide an important reference for seismic design of caverns under different seismic environments.

5.4 Aftershock fragility analysis associated with damage states

Based on the numerical results from 1056 nonlinear dynamic analyses, this section further investigates the evolution of damage states of underground caverns in different mainshock-induced damage states under the re-excitation of aftershocks. Figure 11 illustrates the relationship between the mainshock damage index DS_M and the mainshock–aftershock cumulative damage index DS_{MA}. For both NFMA and FFMA, the data points exhibit a clear upward trend, indicating that as the initial damage induced by the mainshock increases, the cumulative damage after the aftershock also correspondingly increases. This demonstrates that the final damage state of underground caverns is determined not only by the intensity of the aftershock but also strongly influenced by the initial damage level caused by the mainshock. From the distribution characteristics of the scatter plots, it can be seen that the vast majority of data points are located above the 45-degree diagonal line ($DS_M = DS_{MA}$), directly confirming the amplifying effect of aftershocks on cavern damage. Moreover, even under the same level of mainshock damage, the cumulative damage index DS_{MA} exhibits different evolutionary patterns with increasing mainshock damage. This phe-

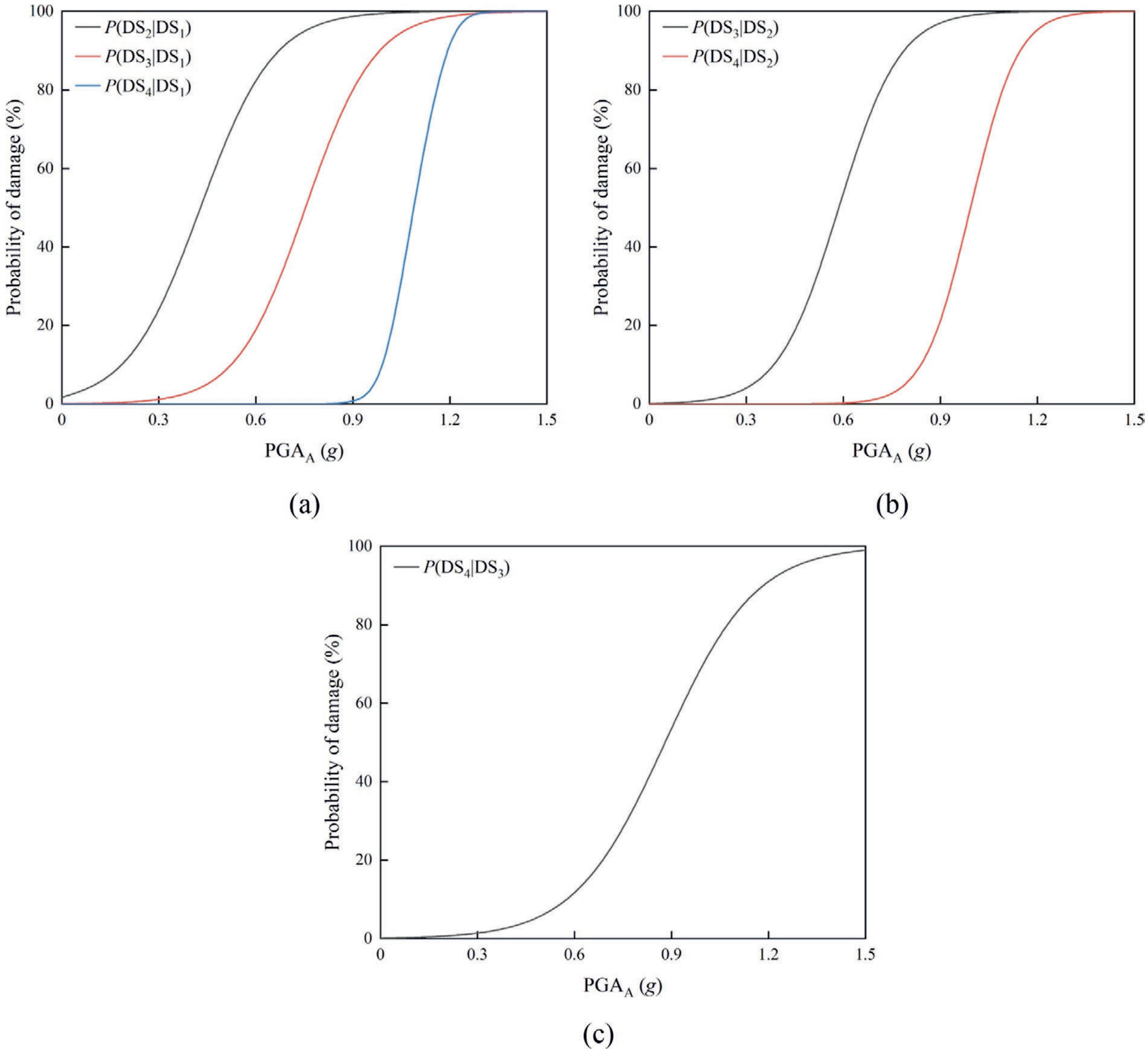

Fig. 12. Aftershock fragility curves for different damage levels under the same DS_M state of NFMA. (a) $DS_M = DS_1$, (b) $DS_M = DS_2$, and (c) $DS_M = DS_3$.

nomenon indicates that aftershocks are not simply linearly superimposed on the existing damage but involve complex nonlinear cumulative effects.

Comparing Fig. 11(a) and (b), it can be observed that under NFMA, the data points are concentrated in the severe damage region DS_3, whereas under far-field ground motions, the data points are mainly distributed in the slight damage DS_1 and moderate damage DS_2 regions. This indicates that NFMA tends to induce more severe initial damage during the mainshock stage. Furthermore, within the DS_1 and DS_2 regions of the mainshock, a higher proportion of data points under NFMA show transitions from DS_1 in the mainshock to DS_2 and DS_3 in the mainshock–aftershock sequence, as well as from DS_2 in the mainshock to DS_3 in the sequence. This finding demonstrates that NFMA also exhibits a stronger cumulative damage capability during the aftershock stage.

Section 5.3 focuses on analyzing the probabilities of underground caverns reaching different damage limit states under mainshock–aftershock sequences. To quantitatively reveal the effect of aftershocks on cavern damage evolution, aftershock fragility curves are constructed for different limit states DS_{MA} corresponding to the same mainshock damage state DS_M. The aftershock fragility curves under NFMA and FFMA are shown in Figs. 12 and 13, respectively.

From the aftershock fragility curves corresponding to different mainshock damage states ($DS_M = DS_1$, DS_2, DS_3), it can be observed that the curves for NFMA exhibit a steeper shape compared to those for FFMA. Moreover, the fragility curves are overall shifted closer to the left side of the horizontal axis under NFMA, indicating that NFMA is more likely to induce state transitions in underground caverns under the same aftershock intensity. For instance, when the PGA_A under NFMA is 0.9*g*, if the mainshock-damaged cavern is in a slight damage state DS_1, the probabilities of transitioning to moderate damage DS_2, severe damage DS_3, and collapse DS_4 after the

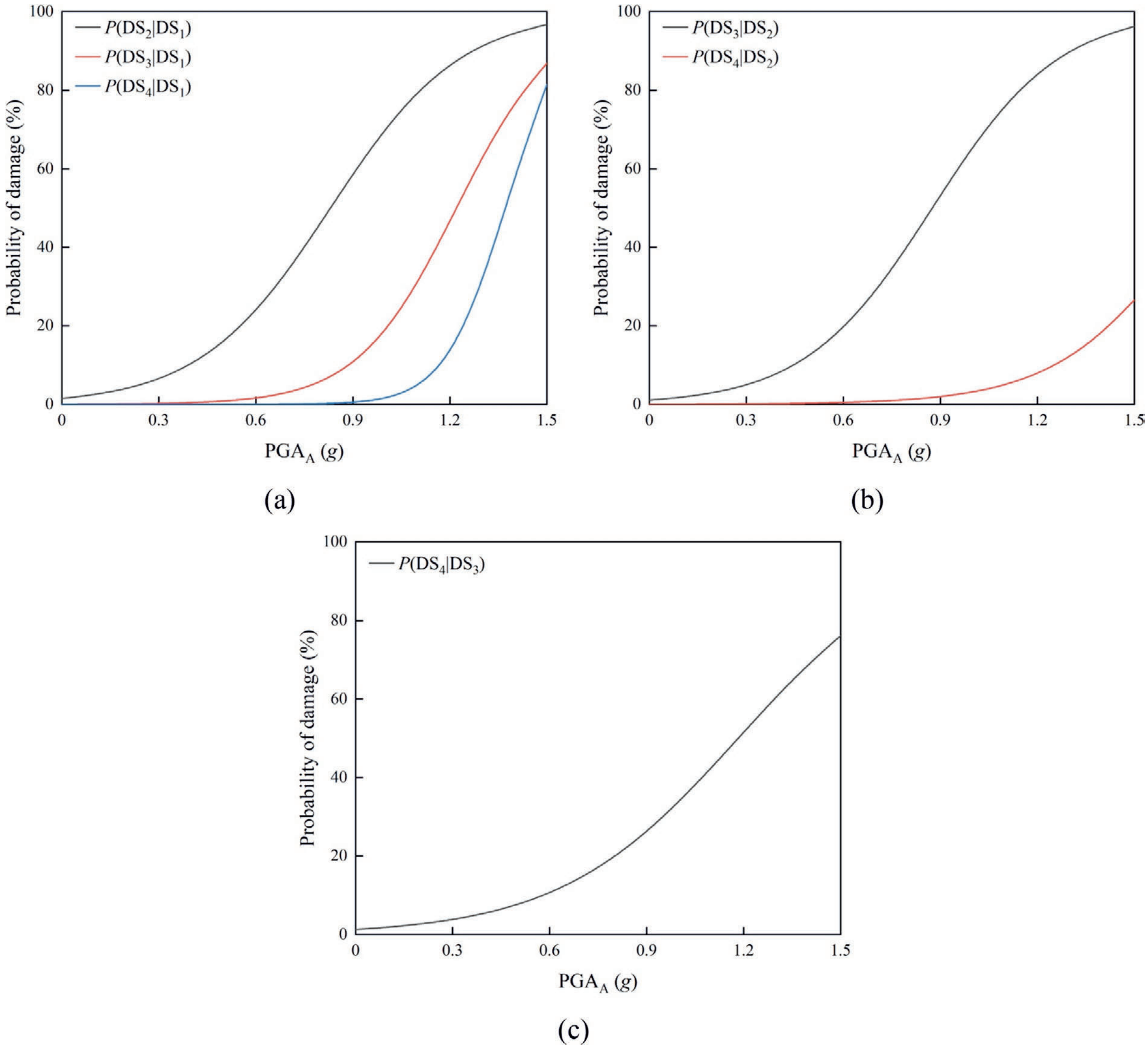

(a)

(b)

(c)

Fig. 13. Aftershock fragility curves for different damage levels under the same DS_M state of FFMA. (a) $DS_M = DS_1$, (b) $DS_M = DS_2$, and (c) $DS_M = DS_3$.

aftershock are 98.56%, 79.74%, and 0.76%, respectively. If the mainshock-damaged cavern is in a moderate damage state DS_2, the probabilities of transitioning to DS_3 and DS_4 after the aftershock are 96.95% and 21.12%, respectively. If the mainshock-damaged cavern is in a severe damage state DS_3, the probability of transitioning to collapse DS_4 after the aftershock reaches 53.51%. By contrast, under FFMA with PGA_A of 0.9*g*, if the mainshock-damaged cavern is in a slight damage state DS_1, the probabilities of transitioning to DS_2, DS_3, and DS_4 after the aftershock are 58.21%, 10.58%, and 0.53%, respectively. If the mainshock-damaged cavern is in a moderate damage state DS_2, the probabilities of transitioning to DS_3 and DS_4 after the aftershock are 53.06% and 1.95%, respectively. If the mainshock-damaged cavern is in a severe damage state DS_3, the probability of transitioning to DS_4 after the aftershock is 26.17%.

These results indicate that caverns in damaged states after mainshocks can readily transition into more severe damage states under aftershock excitations. Moreover, as the mainshock-induced damage level increases, the seismic redundancy of cavern decreases significantly, and brittle failure characteristics under aftershocks become more pronounced. Particularly, when the cavern reaches the severe damage state DS_3 after the mainshock, even relatively small aftershock intensities may trigger catastrophic collapse. This pattern of cumulative damage and state transitions highlights the progressive failure mechanism of underground caverns under sequential seismic actions and reveals the state-dependent characteristics of damage accumulation following the mainshock. The distinct differences in aftershock fragility characteristics between NFMA and FFMA further underscore the importance of considering ground motion type characteristics in the seismic design of underground structures.

6 Conclusions

This study establishes a probabilistic seismic fragility framework that incorporates ground motion type and sequence characteristics. Based on extensive nonlinear dynamic analyses, the following principal conclusions are drawn:

(1) The surrounding rock of underground caverns exhibits significant cumulative damage effects under mainshock–aftershock sequences. As the PGA_A increases, both the residual displacement and RFD of the underground cavern group further increase. Particularly under high-intensity mainshocks ($\geq 0.8g$) and strong aftershocks, the failure distribution pattern of the cavern transitions from uniform to non-uniform. The surrounding rock of the caverns exhibits RFD banding expansion and tends to connect, with significant residual displacement peak phenomena observed around caverns, showing typical non-linear cumulative damage characteristics.

(2) Comparative analysis of RFD and residual displacement distributions under NFMA/FFMA reveals that the left arch shoulder and right arch foot of the main powerhouse, as well as the arch foot and sidewall of the main transformer chamber, exhibit deeper RFD extension, indicating potential weak zones in seismic design, which should be given priority for strengthened support. Furthermore, NFMA has greater destructiveness to underground caverns than to FFMA.

(3) The impact of aftershocks on cavern fragility cannot be ignored, as the fragility probability of underground caverns increases significantly with aftershock excitation. For NFMA (α = 0.8–1.2), each 0.1*g* increase in PGA_A results in average exceedance probability increases of 54.74%, 46.55%, and 38.10% for underground caverns in OP, RP, and LS states, respectively, which is significantly higher than that of FFMA. This indicates that methods considering only mainshocks significantly underestimate the instability probability of caverns under sequence-type ground motions.

(4) Aftershock fragility is strongly related to the mainshock-damaged state for underground caverns. With the increase in the mainshock-damaged state of the underground cavern, the probability of reaching the same DS_{MA} under equivalent PGA_A is significantly increased. The collapse probability of underground caverns after 0.9*g* aftershocks in NFMA increased from 0.76% in DS_1 to 21.12% in DS_2 and 53.51% in DS_3. Under the same PGA_A in FFMA, the collapse probability increased from 0.53% in DS_1 to 1.95% in DS_2 and 26.17% in DS_3. This highlights the urgent need for fragility reassessment after the mainshock.

(5) Ground motion type has a significant impact on the seismic stability assessment of underground caverns. Compared to FFMA, fragility curves under NFMA exhibit obvious overall “leftward shift” phenomena, indicating that NFMA has a higher probability of causing various damage levels of underground caverns. Specifically, the NFMA shows average probability increases of 14.46%, 15.44%, 16%, and 20.00% compared with the FFMA under the four conditions of only mainshock, $\alpha = 0.8$, $\alpha = 1.0$, and $\alpha = 1.2$, respectively. Therefore, in the seismic performance evaluation and design of underground caverns located in near-fault regions, it is essential to fully consider the unique damage characteristics of near-fault ground motions and the cumulative damage effects induced by mainshock–aftershock sequences.

This study provides a comprehensive fragility framework, but it also has certain limitations. Firstly, the analysis relies on numerical simulation, and its accuracy depends on the constitutive model and parameters adopted. Compared with the empirical methods directly derived from on-site damage data, although our method is very effective for scenario analysis and inference, it needs to be carefully calibrated to ensure authenticity. Moreover, strong earthquakes are often accompanied by multiple aftershocks. In this study, only the mainshock + single aftershock sequence is considered, and the potential cumulative damage and fragility analysis under the mainshock + multiple aftershock sequence needs further study.

Data availability

The data that support the findings of this study are available from the corresponding author upon reasonable request.

CRediT authorship contribution statement

Pengfei Chen: Writing – original draft, Formal analysis, Data curation. **Quan Jiang:** Writing – review & editing, Methodology, Funding acquisition, Conceptualization. **Yong Xia:** Resources, Data curation. **Zhijun Liu:** Resources, Data curation. **Long Li:** Validation, Software.

Declaration of competing interest

The authors declare that they have no known competing financial interests or personal relationships that could have appeared to influence the work reported in this paper.

Acknowledgement

The authors gratefully acknowledge the financial support from the National Natural Science Foundation of China (Grant Nos. 52325905 and U25B20222) and Key Technology Research Projects of Power China (Grant Nos. DJ-HXGG-2023-16 and DJ-HXGG-2023-04). Data of Luding ground motion for this study are provided by the Institute of Engineering Mechanics, China Earthquake Administration.

References

An, X. H., Shawky, A. A., & Meaekawa, K. (1997). The collapse mechanism of a subway stationduring the great hanshin earthquake. *Cement and Concrete Composites, 19*(3), 241–257.

Antoniou, M., Mantakas, A., Nikitas, N., & Fuentes, R. (2023). A numerical case study on the long-term seismic assessment of reinforced concrete tunnels in corrosive environments. *Journal of Rock Mechanics and Geotechnical Engineering, 15*(3), 551–572.

Bath, M. (1965). Lateral inhomogeneities of the upper mantle.pdf. *Tectonophysics, 2*(6), 483–514.

Bigdeli, A., Vosoughi, S., Tsavdaridis, K. D., Eslamnia, H., & Farajian, M. (2025). Seismic risk assessment of steel volumetric modular buildings under the mainshock-aftershock ground motions. *Structures, 76*, 108960.

Chen, P. F., Jiang, Q., Liu, J., Li, S. J., Chen, T., & He, B. G. (2024). Global stability coefficient of large underground caverns under static loading and earthquake wave condition. *Journal of Central South University, 31*(8), 2826–2843.

Chen, P. F., Jiang, Q., Xiang, T. B., Xia, Y., & Hou, D. Q. (2025). Seismic impact of mainshock-aftershock sequences on underground caverns: A case study of dynamic response. *Engineering Failure Analysis, 167*, 109072.

Chen, P. L., Geng, P., Chen, J. B., & Gu, W. Q. (2023). The seismic damage mechanism of Daliang tunnel by fault dislocation during the 2022 Menyuan Ms6.9 earthquake based on unidirectional velocity pulse input. *Engineering Failure Analysis, 145*, 107047.

Cui, C. Y., Xu, M. Z., Xu, C. S., Zhang, P., & Zhao, J. T. (2023). An ontology-based probabilistic framework for comprehensive seismic risk evaluation of subway stations by combining Monte Carlo simulation. *Tunnelling and Underground Space Technology, 135*, 105055.

Cui, C. Y., Zhao, J. T., Xu, M. Z., Xu, C. S., Liu, H. L., & Wang, K. P. (2025). Multidimensional seismic fragility analysis of subway station structures using the adaptive bandwidth kernel density estimation and Copula function. *Underground Space, 22*, 110–123.

Feng, X. T., Yang, C. X., Kong, R., Zhao, J., Zhou, Y. Y., Yao, Z. B., et al. (2022). Excavation-induced deep hard rock fracturing: Methodology and applications. *Journal of Rock Mechanics and Geotechnical Engineering, 14*(1), 1–34.

Fu, J., Chen, Y. G., Nie, Q. X., Lv, Z. P., & Li, J. W. (2025). Source modeling of the 2023 Herat earthquake sequence determined from InSAR observations. *Geodesy and Geodynamics, 16*(5), 624–634.

Guo, Z. K., Han, J. Y., El Naggar, M. H., Bi, Y. S., Xu, C. S., & Du, X. L. (2024). Vector-valued fragility analysis of subway station structures subjected to the Kahramanmaras earthquake. *Soil Dynamics and Earthquake Engineering, 182*, 108739.

Huang, Z. K., Zhang, D. M., Zhang, W. Y., & Li, Y. B. (2025). Impact of ground motion characteristics on the seismic fragility of circular tunnels. *Underground Space, 24*, 180–196.

Jaramillo, C. A. (2017). Impact of seismic design on tunnels in rock – Case histories. *Underground Space, 2*(2), 106–114.

Jiang, Q., Feng, X. T., Li, S. J., Su, G. S., & Xiao, Y. X. (2019). Cracking-restraint design method for large underground caverns with hard rock under high geostress condition and its practical application. *Chinese Journal of Rock Mechanics and Engineering, 38*(6), 1081–1101.

Jiang, Q., Yang, Y., Yan, F., Zhou, J. B., Li, S. J., Yang, B., et al. (2021). Deformation and failure behaviours of rock-concrete interfaces with natural morphology under shear testing. *Construction and Building Materials, 293*, 123468.

Liu, C. X., Zhang, F. S., Wang, Q., Wang, B., Zhang, Q., & Xu, B. (2023). Evaluation of fault stability and seismic potential for Hutubi underground gas storage due to seasonal injection and extraction. *Underground Space, 13*, 74–85.

Liu, J. C., Meng, X. R., Tian, L., Yang, M., Jin, Q. T., & Shao, G. D. (2024). Multi-metric evaluation of the optimal intensity measure for mainshock-aftershock fragility analysis of transmission towers. *Engineering Structures, 308*, 118020.

Liu, Q., Zhang, X. W., Jiang, Q., Xia, Y., Hou, D. Q., & Li, L. (2025). Effects of nano-Al2O3 nano-MgO and nano-Fe2O3 on the properties of cement-based 3D printing: A comparative study. *Journal of Building Engineering, 111*, 113322.

Lozos, J. C., & Harris, R. A. (2020). Dynamic rupture simulations of theM6.4 andM7.1 July 2019 ridgecrest, California, Earthquakes. *Geophysical Research Letters, 47*(7).

Lv, T., Li, H. B., Yang, J. H., Zhou, Q. Q., & Li, J. R. (2009). Comparison between 2D and 3D numerical analysis for seismic response of Xiluodu underground caverns. *Rock and Soil Mechanics, 30*(3), 7211–7729 (in Chinese).

Ma, X., Chen, D. D., Xie, S. R., Zou, J., Wu, H. D., Sun, A. G., et al. (2025). Failure mechanism of severe deformation in gob-side entry rib and unloading-supporting coupling control technology. *Engineering Failure Analysis, 167*, 108973.

Meng, S. B., Li, W. X., Liu, Z. X., Liu, J. Q., He, W. G., Yang, C. W., et al. (2024). Rapid resilience assessment framework for mountain tunnels subjected to near-fault seismic ground motions. *Soil Dynamics and Earthquake Engineering, 182*, 108746.

Nouri, G., Rayegani, A., Lavasani, H. H., Tavakoli, L., Nasiri, M., & Soureshjani, O. K. (2023). Seismic performance of the RBS connection with trapezoidal corrugated web (TCW-RBS). *Structures, 56*, 105003.

Pu, W. C., & Li, Y. H. (2023). Evaluating structural failure probability during aftershocks based on spatiotemporal simulation of the regional earthquake sequence. *Engineering Structures, 275*, 115267.

Qiu, D. P., Chen, J. Y., & Xu, Q. (2019). 3-D numerical analysis on seismic responses of the underground large scale frame structure under near-fault ground motions. *Tunnelling and Underground Space Technology, 91*, 103020.

Rayegani, A., Soureshjani, O. K., Alaee, S. A. M., Mualla, I. H., & Nemati, F. (2024). Seismic performance of buildings equipped with four-joint rotational friction dampers in mainshock–aftershock sequences. *Journal of Structural Engineering, 150*(3), 04023235.

Sasmi, A. T., Nugraha, A. D., Muzli, M., Widiyantoro, S., Syuhada, S., Muttaqy, F., et al. (2023). Shear wave splitting of the 2018 lombok earthquake aftershock area. *Indonesia. Geoscience Letters, 10*(1).

Shen, Y. S., Gao, B., Yang, X. M., & Tao, S. J. (2014). Seismic damage mechanism and dynamic deformation characteristic analysis of mountain tunnel after Wenchuan earthquake. *Engineering Geology, 180*, 85–98.

Shimizu, M., Suzuki, T., Kato, S., Kojima, Y., Yashiro, K., & Asakura, T. (2007). Historical earthquake damage to tunnels in Japan and case studiesof railway tunnels in the 2004 Niigataken-Chuetsu earthquake. *Quarterly Report of RTRI, 48*(3), 136–141.

Soureshjani, O. K., & Lavassani, S. H. H. (2023). Performance of tuned particle impact damper and tuned mass damper seismic control systems considering mainshock-aftershock. *Structures, 56*, 104924.

Soureshjani, O. K., & Massumi, A. (2019). Effect of near and far-field earthquakes on RC bridge with and without damper. *Earthquakes and Structures, 17*(6), 533–543.

Stewart, J. P., Chiou, S. J., Bray, J. D., Graves, R. W., Somerville, P. G., & Abrahamson, N. A. (2002). Ground motion evaluation procedures for performance-based design. *Soil Dynamics and Earthquake Engineering, 22*(9/10/11/12), 765–772.

Sun, B. B., Zhang, S. R., Deng, M. J., & Wang, C. (2020). Nonlinear dynamic analysis and damage evaluation of hydraulic arched tunnels under mainshock–aftershock ground motion sequences. *Tunnelling and Underground Space Technology, 98*, 103321.

Sun, R. F., Xu, H., Yan, Q. X., Yang, K., & Zhang, C. (2024). Effects of seismic buffer thickness on a circular rock tunnel considering seismic damage form and failure state. *International Journal of Rock Mechanics and Mining Sciences, 183*, 105892.

Wang, Z. Z., Gao, B., Jiang, Y. J., & Yuan, S. (2009). Investigation and assessment on mountain tunnels and geotechnical damage after the Wenchuan earthquake. *Science in China Series E: Technological Sciences, 52*(2), 546–558.

Xu, M. Z., Cui, C. Y., Zhao, J. T., Xu, C. S., & Meng, K. (2025). A novel approach to seismic fragility evaluation of underground structures considering hybrid epistemic uncertainties of both seismic demand and capacity. *Tunnelling and Underground Space Technology, 156*, 106278.

Xu, M. Z., Cui, C. Y., Zhao, J. T., Xu, C. S., Zhang, P., & Su, J. (2024). Fuzzy seismic fragility analysis of underground structures considering multiple failure criteria. *Tunnelling and Underground Space Technology, 145*, 105614.

Xue, Y. D., Zhang, S., Zhou, M. L., & Zhu, H. H. (2021). Novel SfM-DLT method for metro tunnel 3D reconstruction and Visualization. *Underground Space, 6*(2), 134–141.

Yu, H., & Chen, G. (2021). Pseudo-static simplified analytical solution for seismic response of deep tunnels with arbitrary cross-section shapes. *Computers and Geotechnics, 137*, 104306.

Zhang, L. X., Zhu, B. J., Xue, Y. Q., & Ma, J. L. (2019). Cumulative damage effects of mainshock-aftershock sequences on RC-frame structures. *Earthquake Science, 32*(3/4), 157–169.

Zhao, D. P., & Liu, X. (2016). Crack mystery of the damaging Kumamoto earthquakes. *Science Bulletin, 61*(11), 868–870.

Zhu, R. Z., Guo, T., Xu, G., Zhang, R. J., & Tesfamariam, S. (2025). XGBoost-based probabilistic residual displacement demand prediction for self-centering viscous systems under near-fault ground motions. *Journal of Building Engineering, 111*, 113572.